Journal of the
Meteorological
Society of
Japan

EARLY ONLINE RELEASE

The DOI for this manuscript is
DOI:10.2151/jmsj.2021-007
J-STAGE Advance published date: November 12th, 2020

The impact of diurnal precipitation over Sumatra Island, Indonesia, on synoptic disturbances and its relation to the Madden-Julian Oscillation

Ayako SEIKI, Satoru YOKOI,

Dynamic Coupling of Ocean-Atmosphere-Land Research Program, Research Institute for Global Change, Japan Agency for Marine-Earth Science and Technology, Yokosuka, Japan

and

Masaki KATSUMATA

Global Ocean Observation Research Center, Research Institute for Global Change, Japan Agency for Marine-Earth Science and Technology, Yokosuka, Japan

Submitted in May, 2020
Revised in August, 2020
Accepted in October, 2020

---

1) Corresponding author: Ayako Seiki Japan Agency for Marine-Earth Science and Technology, 2-15, Natsushima-cho, Yokosuka, Kanagawa 237-0061 JAPAN.
Email: aseiki@jamstec.go.jp
Tel: +81-46-867-9825
Fax: +81-46-867-9255

Abstract

The impact of diurnal precipitation over Sumatra Island, the Indonesian Maritime Continent (MC), on synoptic disturbances over the eastern Indian Ocean is examined using high-resolution rainfall data by the Global Satellite Mapping of Precipitation project and the Japanese 55-year Reanalysis data during the rainy season from September to April for the period 2000–2014. When the diurnal cycle is strong, the high precipitation area observed over Sumatra in the afternoon migrates offshore during night-time and reaches 500 km off the coast on average. The strong diurnal events are followed by the development of synoptic disturbances over the eastern Indian Ocean for several days, and apparent twin synoptic disturbances straddling the equator develop only when the convective center of the Madden-Julian Oscillation (MJO) lies over the Indian Ocean (MJO-IO). Without the MJO, the synoptic disturbances develop mainly south of the equator. The differences in the locations and behaviors of active synoptic disturbances are related to the strength of mean horizontal winds in the lower troposphere. During the MJO-IO, the intensification of mean northeasterly winds in the northern hemisphere blowing into the organized MJO convection in addition to mean southeasterly winds in the southern hemisphere facilitate the formation of the twin disturbances. These results suggest that seed disturbances arising from the diurnal offshore migration of precipitation from Sumatra develop differently depending on the mean states over the eastern Indian Ocean. Furthermore, it is shown that the MJO events with the strong diurnal cycle tend to have longer duration and continuing eastward propagation of active convection across the MC whereas the convective activities of the other MJO events weaken considerably over the MC and develop again over the western Pacific. These results suggest that the strong diurnal cycle over Sumatra facilitates the smooth eastward propagation of the intraseasonal convection across the MC.

Keywords the Maritime Continent; diurnal cycle; synoptic disturbances; the Madden-Julian Oscillation

1. Introduction

The Indo-Pacific Maritime Continent (MC) consists of a number of islands and seas around the equator and is located in the center of the tropical warm pool. It has been known as the greatest energy source for global atmospheric circulation because significant amounts of heat are released through heavy rainfall (e.g., Ramage 1968). A large-scale ascending air current associated with active convection over the MC constitutes an essential part of the Walker circulation, linking to the El Niño southern oscillation (ENSO) variability (e.g., Yamanaka 2016).

The diurnal cycle is a fundamental mode of tropical atmospheric variability especially over land primarily driven by insolation. Previous studies have shown that precipitation maxima tend to occur in the late afternoon over land and in the early morning over the open oceans, via analyses of in situ observation data (e.g., Gray and Jacobson 1977), geostationary satellite data (e.g., Albright et al. 1985; Murakami 1983; Nitta and Sekine 1994), and space-borne precipitation radar data (e.g., Takayabu 2002; Nesbitt and Zipser 2003; Kikuchi and Wang 2008) whereas there are some dependencies on regional, topographical, and interannual conditions. Whereas anomalous dry (wet) conditions are found during El Niño (La Niña) over the MC as a whole, dependency of the strength of the diurnal cycle of precipitation on ENSO has regional differences due to topography (e.g., Qian et al. 2010; Rauniyar and Walsh 2013; Qian et al. 2013).

The strong diurnal signal over land in the late afternoon has been observed to be spread out over the adjacent oceans during the night (e.g., Yang and Slingo 2001), but a mechanism of the nighttime offshore migration remains elusive. Several studies have focused on a role of gravity waves emanating from convective system or nighttime radiative cooling over land (e.g., Mapes 2003; Love et al. 2011; Yokoi et al. 2017); others have proposed gravity currents as a cause of the offshore convection through horizontal convergence associated with environmental winds (e.g., Houze et al. 1981; Mori et al. 2004; Yokoi et al. 2019). Yokoi et al. (2017, 2019) examined the diurnal cycle using the data during the two field campaigns in the western coastal region of Sumatra as part of the Years of the Maritime Continent (YMC) project and showed that gravity waves are important to destabilize the lower troposphere before the arrival of the precipitation area whereas vertical shear of horizontal wind near the surface over the coastal waters is another important factor for the migration. In the MC, outstanding diurnal signals accompanied by the nighttime offshore migration were found in the western coast of Sumatra Island (e.g., Mori et al. 2004; Sakurai et al. 2005), in the northwestern coast of Borneo Island (e.g., Houze et al. 1981; Ichikawa and Yasunari 2006), and in New Guinea Island (e.g., Liberti et al. 2001; Zhou and Wang 2006; Ichikawa and Yasunari 2008). Among them, this study focuses on the diurnal signals over and around Sumatra Island.

Because the MC convection and its variability play essential roles in the global climates as mentioned above, it seems important for general circulation models (GCMs) to realistically simulate precipitation and convection over the MC. However, the models suffer from significant errors and cannot reproduce the observed diurnal cycle, partly due to their coarse resolution (e.g., Neale and Slingo 2003; Love et al. 2011). The complex topography including small islands and semi-enclosed seas of the MC cannot be resolved by the GCMs, leading to unrealistic simulations. The difficulty in simulating the diurnal cycle over the MC may influence the reproducibility of another dominant atmospheric mode at intraseasonal time scales in the tropics, which is called the Madden-Julian Oscillation (MJO; e.g., Madden and Julian 1971, 1972, 1994; Zhang 2005). The MJO has been known to propagate eastward around the equator with a period of 30-40 days accompanied by deep cumulus convection over the warm pool. Although the MJO has been recognized as a planetary scale disturbance, it has a hierarchal structure composed of eastward-propagating cloud clusters and westward-propagating synoptic disturbances (e.g., Nakazawa 1988). The GCMs have particular difficulty in reproducing the MJO propagation around the MC in addition to their poor representation of the MJO itself. Observational studies have shown that the MJO often weakened and sometimes ceased when it passed over the MC (e.g., Wang and Rui 1990; Matthews 2008). This disruption of the MJO propagation over the MC is known as a barrier effect of the MC and is exaggerated in many GCMs, making the MJO prediction increasingly difficult (e.g., Kim et al. 2009; Seo et al. 2009; Vitart and Molteni 2010). Previous studies have suggested several possible reasons for the MC barrier effect such as the topographic blocking and moisture advection (e.g., Inness and Slingo 2006; Wu and Hsu 2009; Kim et al. 2017; Zhang and Ling 2017). Another possible reason for the MC barrier effect is the interaction between the diurnal cycle and the MJO. Hagos et al. (2016) has shown using a cloud-permitting regional model that the MJO convective signals propagating the MC are stronger in runs without the diurnal forcing compared to those in runs with the diurnal forcing. Majda and Yang (2016) suggested that the diurnal cycle might cause the stalled or suppressed propagation of the MJO across the MC using a simple multiscale model.

It is well known that the MJO acts to modulate the diurnal cycle. However, which phases accompany the strong diurnal cycle over the MC is still controversial. Several studies have shown that the diurnal cycle over the MC is enhanced during the convectively active phase of the MJO (e.g., Tian et al. 2006; Ichikawa and Yasunari 2007), whereas others have found pronounced diurnal cycle over the MC during the suppressed phase, just before the arrival of the active phase (e.g., Fujita et al. 2011; Peatman et al. 2014; Birch et al. 2016). Rauniyar and Walsh (2011) has also indicated that mean and diurnal rainfall over the MC land regions reach their peaks during the suppressed phase but those over surrounding seas attain their maxima during the active phase.

Whereas many previous studies so far have investigated the modulation of the diurnal cycle over the MC by the MJO, upscale effects of the diurnal cycle remain largely unexplored, especially the effects on synoptic scale disturbances. Since the MJO has the hierarchal structure, as mentioned above, such effects on the synoptic disturbances embedded in the MJO might modulate the MJO itself. In this study, the impact of diurnal precipitation over Sumatra Island on synoptic disturbances over the eastern Indian Ocean, and its relation to the MJO will be examined using global precipitation datasets.

The rest of this paper is organized as follows. The datasets and methodology are described in Section 2. Section 3 provides general features of the diurnal events over Sumatra detected in this study. In Sections 4 and 5, we investigate the development of synoptic disturbances over the Indian Ocean during the diurnal events and its relationship to the MJO phase and intensity. The mechanisms responsible for the development of synoptic disturbances are examined in Section 6. The influence of the diurnal events on the MJO propagation is discussed in Section 7. The final section provides a summary.

2. Data and methodology

High-resolution hourly rainfall data with a horizontal resolution of 0.1° obtained from satellite-borne microwave radiometers by the Global Satellite Mapping of Precipitation (GSMaP) project (Kubota et al. 2007; Aonashi et al. 2009) are used to investigate the diurnal cycle for the period March 2000–February 2014. We use the reanalysis version (GSMaP_RNL), which is processed same as the standard version (GSMaP_MVK ver. 7) but available for a longer period (Kubota et al. 2020). We focus on the Indonesian rainy season from September to April, defined broadly since there are regional differences within the MC (e.g., Hamada et al. 2002).

Synoptic disturbances and mean states are examined using mean-daily reanalysis data recorded four times daily on 1.25° × 1.25° grids obtained from the Japanese 55-year

Reanalysis (JRA55; Kobayashi et al. 2015) provided by the Japan Meteorological Agency. Zonal and meridional winds (*u* and *v*), vertical velocity (*ω*), pressure (*p*), temperature (*T*), and geopotential (*Φ*) at pressure levels from 1000 to 100 hPa are used. In addition, daily optimum interpolation SST high-resolution datasets, provided by the National Oceanic and Atmospheric Administration (NOAA)/Office of Oceanic and Atmospheric Research/Earth System Research Laboratory, Physical Sciences Division, on 0.25° × 0.25° grids (Reynolds et al. 2007) are used.

As a proxy for large-scale convective activities associated with the MJO, NOAA daily outgoing long-wave radiation (OLR) data on 2.5° × 2.5° grids (Liebmann and Smith 1996) are used. For the MJO index, an all-season real-time multivariate MJO (RMM) index (Wheeler and Hendon 2004) is applied, which is composed of a leading pair of empirical orthogonal functions combining the fields of near-equatorial OLR and zonal winds in the lower and upper troposphere. The amplitude and phases of the MJO are determined using the pair of principal component time series, RMM1 and RMM2. The MJO events in this study are identified when the amplitude of the RMM index exceeds 1.0 for consecutive 15 days. The average amplitude of the RMM index over the rainy season (September–April) of the study period (March 2000–February 2014) is 1.29 and the standard deviation is 0.66. Therefore, we can say that the MJO is inactive when the amplitude of the RMM index is less than 0.63 corresponding to mean minus one standard deviation.

In this study, statistical significances of the differences of various composite means from respective averages over the rainy season of the study period, and those of the difference of composite anomalies from zero, are examined using the Student's t test.

3. Strong diurnal events over Sumatra Island

To examine the diurnal cycle of precipitation, precipitation r at each grid point is fitted to a curve of the form

$$\mathrm{r} = \bar{r} + A\cos\left\{\frac{2\pi}{\tau}(t - t_0)\right\}$$

where $\bar{r}$ is the daily mean precipitation, A is the amplitude of the diurnal harmonic, τ =24 hours is the time period of the diurnal harmonic, and t_0 is a time offset (Love et al. 2011; Peatman et al. 2014). The t_0 is assumed to be constant and determined for each grid point as the time with the maximum in mean diurnal cycle of precipitation averaged over the rainy season of the study period. Figure 1 (upper) shows the mean amplitude of the diurnal harmonic A averaged over the rainy season. Strong diurnal signals of precipitation are found in the western coast of Sumatra Island, the southern coast of Java Island, the northwestern coast of Borneo Island, and the southeastern coast of Sulawesi Island, consistent with previous studies (e.g., Mori et al. 2004; Ichikawa and Yasunari 2006; Love et al. 2011). Figure 1 (lower) shows the local time of mean maximum precipitation, t_0. The maximum precipitation is found from midafternoon to night over land, and extends toward coastal sea regions from midnight to early morning. Whereas the peak time is uniform and parallel to the coastline over land and coastal regions, the distributions over the open ocean are scattered, indicating that this analysis is applicable only for land and coastal regions.

To examine influence of the diurnal cycle, we compare days with vigorous diurnal cycle with those without it. For this purpose, we define strong (weak) diurnal events over Sumatra Island as days when the three-day running mean amplitude of the diurnal harmonic A averaged over the Sumatra area (95°E–105°E, 5°N–5°S) represented by a square in Fig. 1 becomes more (less) than mean plus (minus) one standard deviation. A sequence of the diurnal events is counted as one event, and the first day is used for the reference day of the events in a following composite analysis. The number and average duration of the strong (weak) diurnal events is 132 (78) and 2.84 (3.36) days, respectively. We focus mainly on the strong diurnal events to elucidate its impact on the larger scale phenomena.

Figure 2 shows the monthly number of the strong diurnal events over the Sumatra area (black bars) and accumulated days of the strong diurnal events (gray bars) on the left ordinate. The diurnal events occur most frequently in October and November and decrease drastically from December to January. The frequency of the diurnal events varies in parallel with monthly mean precipitation amount averaged over the Sumatra area (solid line), with a correlation coefficient of 0.90. In addition, the ratio of precipitation amount during the strong diurnal events to the total amount (dashed line) reaches almost 40% in October and November when the strong diurnal events frequently occur. On the other hand, mean amplitude of the diurnal events (dotted line) shows almost the same value among months. These results indicate that the diurnal precipitation is the dominant contributor to the mean precipitation, consistent with previous studies (e.g., Peatman et al. 2014). In December, the number of the diurnal events and the ratio of the diurnal precipitation amount decrease drastically compared to October–November, whereas the mean precipitation values are comparable. This may indicate that the contribution of precipitation related to synoptic or intraseasonal disturbances such as the MJO to the mean precipitation is relatively large in December and small in October. In fact, the MJO is most active in December (e.g., Madden 1986; Zhang and Dong 2004).

First, we compare the daily mean precipitation between the strong and weak diurnal events (Fig. 3). Much higher precipitation amounts, corresponding to large condensation heating, around the western coast of Sumatra are found during the strong diurnal events, consistent with results in Mori et al. (2004) and Love et al (2011). During the strong (weak) diurnal events, the precipitation amount averaged over the Sumatra area starts to increase (decrease) on day −2 and reaches the maximum (minimum) on day +1. Note that the first day, not the day of the maximum amplitude, is used for the reference day as mentioned previously.

Figure 4 depicts the composite diurnal precipitation over and around Sumatra Island for the strong diurnal events on day 0, while Fig. 5 shows the composite diurnal cycle of precipitation as a function of distance from the coastline. Precipitation increases over the western coast of Sumatra in the evening from 15 LT to 21 LT. Although precipitation amounts over coastal land areas are relatively small compared with the results in Mori et al. (2004), this difference may result from the datasets analyzed; Mori et al. (2004) used the TRMM precipitation radar data while the GSMaP data mainly uses microwave radiometer data. However, further analyses are needed to validate the differences quantitatively. The heavy precipitation area then migrates offshore during nighttime, reaching approximately 500 km off the coast in the next morning. Note that, based on the argument in Ogino et al. (2016), the oceanic area 500 km off the coast can be regarded as the open ocean. The distance of the migration is longer than the results of climatology (Mori et al. 2004), probably because here we examine the strong diurnal events only. There also exists a northeastward migration, but its amplitude is weak and has been known to have strong seasonality (Sakurai et al. 2005). In the next section, we investigate the relationship between the offshore migration of precipitation reaching the open ocean and synoptic disturbances developed over the Indian Ocean.

4. Synoptic disturbances associated with the diurnal events over Sumatra

In the previous section, we found that the diurnal signals of precipitation propagating from Sumatra reach the open ocean. We now consider upscale effects of the strong diurnal cycle on synoptic disturbances over the eastern Indian Ocean. The activity of synoptic disturbances is represented by the eddy kinetic energy (K')

$$\mathrm{K}' = \frac{1}{2}\left(\overline{u'^2} + \overline{v'^2}\right),$$

where u' and v' represent eddy zonal and meridional winds, respectively, defined as the deviation from the 11-day running-mean. Hereafter, the eddy components with a prime represent synoptic time scales and shorter. The mean components, represented with an overbar, are defined as an 11-day running mean indicating intraseasonal time scales and longer. Figure 6 (left) shows the composite K’ at 850 hPa for the strong diurnal events. The K’ values are generally higher over the open oceans such as the Indian Ocean, the South China Sea, and western north Pacific and lower over the MC, especially over land. Over the eastern Indian Ocean, the K’ further increases off Sumatra as time proceeds, which is depicted more clearly in the composite tendency of K’ (dK’/dt) at 850 hPa (Fig. 6, right). When the diurnal signal is strong over Sumatra (day 0), the strongest generation of K’ is found south of the equator off the western coast of Sumatra. The high K’ values extend southwestward and reach the central south Indian Ocean on day +4. A large increase in K’ is also found west of the northern edge of Sumatra around 5°N on day 0. Cyclonic eddies straddling the equator off Sumatra are found corresponding to the area of high K’ generation (Fig. 7). This result indicates that large values of K’ consist of the energy of cyclonic eddies. Time-longitude sections of composite dK’/dt for the strong events (Fig. 8, left) show clear westward migration of the K’ increase from the coastline from day 0 in both hemispheres, suggesting the influence of the diurnal cycle on the development of synoptic disturbances. Whereas the dK’/dt before day 0 is negligible in the northern Indian Ocean, the moderate K’ increase is found in the southern Indian Ocean around 70°E and 95°E from day –4. Slow eastward propagation of a large-scale envelope of the K’ increase suggests some relationship with the MJO consisting of synoptic disturbances, which is examined in detail in the next section. In summary, synoptic disturbances with cyclonic flows develop off the western coast of Sumatra both north and south of the equator and are enhanced over the eastern Indian Ocean with westward and/or poleward migration within several days after the day of the strong diurnal cycle over Sumatra.

To elucidate the impact of the diurnal cycle, the same composites but for the weak diurnal events are shown in the right panel of Fig. 8. The strong K’ generation off Sumatra found in the strong events is not observed in the weak events, instead a K’ decrease dominates over the eastern Indian Ocean from day –4. Differences of dK’/dt between the strong and weak diurnal events (Fig. 9) are statistically significant especially over the eastern Indian Ocean from day 0 and large values shift westward as time proceeds, corresponding to the K’ increase during the strong diurnal events. Given the diurnal offshore migration of precipitation reaching 500 km off the coast (Fig. 5), these differences between the strong and weak diurnal events indicate that the enhancement of synoptic disturbances off Sumatra is connected to the diurnal cycle of precipitation over Sumatra.

5. Interaction with the MJO

As mentioned in the Introduction, the MJO can act to modulate the diurnal cycle over the MC. The diurnal events detected in the previous sections might have dependency on the MJO phases. Figure 10 (left) shows accumulated days of the diurnal events in each MJO phase. Strong diurnal events occur preferentially in the MJO phases 2 and 3 when the active MJO convection is located over the Indian Ocean, consistent with previous studies (e.g., Fujita et al. 2011; Peatman et al. 2014). In addition, a number of the diurnal events are found when the MJO is inactive (Non-MJO). During the phase 1, there are many days when the MJO amplitude exceeds 1.0 (black bars) but most of them did not last for 15 days, resulting in a smaller number of the MJO events (gray bars) compared to the phases 2 and 3. The diurnal events decrease in phase 4 when the MJO convection lies over the MC, which might be related to the weakening of solar radiation by a large amount of clouds. In comparison to the climatology (Fig. 10, right), drastic reductions during the phases 4–8 when the MJO is located over the MC or the Pacific stand out.

One concern arising from the strong dependency of the diurnal cycle on the MJO phases is that the active synoptic disturbances during the strong diurnal events shown in Fig. 6, 7, and 8 (left) include internal synoptic eddies within the MJO convective envelope over the Indian Ocean and may not be triggered solely by the diurnal cycle over Sumatra. Therefore, we classify the diurnal events into three groups according to the MJO amplitude and phases (see section 2 for the MJO definition). The diurnal events when the MJO phases are from 2 to 3 (from 5 to 7) are classified into the MJO-IO (MJO-Pac). The other group is composed of the events when the MJO is inactive (Non-MJO). The numbers of the strong diurnal events during the MJO-IO, MJO-Pac, and Non-MJO are 36, 5, and 20, respectively. The contrast in the number between MJO-IO and MJO-Pac is consistent with the strong dependency of the diurnal cycle on the MJO phase as shown in Fig. 10. Hereafter, composite results for the MJO-IO and Non-MJO are shown since a large part of composite results for the MJO-Pac is not statistically significant due to its few degrees of freedom. This classification is intended to investigate the impact on synoptic disturbances solely by the diurnal signals over Sumatra during the Non-MJO and the interaction between MJO and the diurnal signals through synoptic disturbances during the MJO-IO. Comparison of generation rates of K’ between the MJO-IO and Non-MJO is shown in Figs. 11 and 12. Thick black lines represent proxy for the intraseasonal convective envelope. During the Non-MJO (Fig. 11, right), the K’ is first generated south of the equator on day 0 and spread both north and south of the equator over several days. Although the strong K’ generation is found across the equator off Sumatra, its westward and/or poleward migrations are unclear (Fig. 12, right). In the MJO-IO (Figs. 11 and 12, left), on the other hand, twin disturbances straddling the equator develop off Sumatra and migrate poleward and/or westward rapidly from day 0, resulting in negative values around the equator. The apparent twin synoptic disturbances straddling the equator during the MJO-IO implies the enhancement of the Rossby wave response within the MJO. In addition to the westward migration found from day 0 to +4 off Sumatra, the large-scale K’ generation propagates eastward from the central Indian Ocean to the western Pacific (Fig. 12, left), corresponding to the large-scale intraseasonal convection across the MC shown by black lines. The influence of the diurnal cycle on the eastward-propagation of the MJO will be discussed in Section 7.

We also check the dependency on the MJO in the composites based on the weak diurnal events (not shown). The numbers of the weak diurnal events during the MJO-IO, MJO-Pac, and Non-MJO are 2, 35, and 10, respectively. Compared to the strong events, the percentage of the events during the MJO-Pac (MJO-IO) increases (decreases) drastically, implying the existence of the MJO over the Pacific has great influence on weakening the diurnal events over the MC through large-scale descending branch of the MJO. As shown in composite dK'/dt for all weak diurnal events in Fig. 8 (right), a K' decrease is dominant over the eastern Indian Ocean for the Non-MJO and MJO-Pac. Composite results during the MJO-IO are not statistically significant due to its very few samples.

6. The eddy kinetic energy budget for the strong diurnal events

To understand the mechanisms of the K' generation shown in the previous sections, we consider the budget for K' in the form used in Seiki and Takayabu (2007) and Seiki et al. (2018)

$$\frac{\partial K'}{\partial t} = -\overline{V'_h (V' \cdot \nabla)\overline{V}_h} - \overline{V} \cdot \nabla \overline{K'} - \overline{V' \cdot \nabla K'} - \frac{R}{p}\overline{\omega' T'} - \nabla \cdot (\overline{V' \Phi'}) + D ,$$

KmKe AmKe AeKe PeKe GKe D

where **V** is the three-dimensional velocity vector, $\mathbf{V}_h$ is the horizontal velocity vector, and *R* is the gas constant for dry air. The first term on the right-hand side indicates the barotropic energy conversion to K' from mean kinetic energy (KmKe). The second and third terms represent the advection of K' by the mean flow (AmKe) and the eddy flow (AeKe), respectively. The fourth term is the conversion from eddy available potential energy to K' through the rising or sinking motion of warm or cold air parcels (PeKe), which is related to eddy convective activities. The fifth term denotes the divergence of the eddy geopotential flux (GKe). The last term (D) corresponds to the residuals representing sub-grid-scale effects and dissipation. Since the terms AmKe, AeKe, and GKe mainly describe the redistribution of energy, they are not considered as real sources or sinks. Figure 13a shows the vertical structure of composite means of these terms averaged over the southeastern Indian Ocean area (1.25°S–6.25°S, 92.5°E–102.5°E) for all the strong diurnal events. The dominant contributors are the PeKe, KmKe, GKe, and D terms, which is consistent with previous results investigating synoptic disturbances over the tropical Pacific (e.g., Lau and Lau 1992; Maloney and Dickinson 2003; Seiki and Takayabu 2007; Seiki et al. 2018). Note that similar features are also observed in the composites for the MJO-IO and Non-MJO. The largest energy generation is caused by PeKe around 250 hPa, corresponding to the level of significant diabatic heating by cumulus convective system and ascending motion driven by active synoptic convection (e.g., Nitta 1972; Lau and Lau 1992). This energy generation around 250 hPa is largely offset by GKe, latter of which has positive values above 200 hPa and in the boundary layer. This indicates that the generated K' through PeKe is redistributed to the upper troposphere above 200 hPa and to the boundary layer by eddy divergent flows through GKe. In the lower troposphere, KmKe and GKe around 900 hPa and PeKe around 800 hPa contribute to the large K' increase although the confidence level of PeKe in the lower troposphere is low. The maximum KmKe found in the lower troposphere is related to convergence of mean horizontal winds and the existence of seed eddies, which is explained later. The residual term D is negative at all levels, and its negative maximum is found in the boundary layer at 900 hPa, indicating the large contribution by dissipation. The magnitude of the term D in the boundary layer is much smaller compared to results in previous studies that examine the synoptic disturbances in the generation of equatorial westerly wind bursts over the western Pacific (Seiki and Takayabu 2007; Seiki et al. 2018), suggesting that the synoptic disturbances off Sumatra are not matured.

We focus on the two dominant energy sources, KmKe in the lower troposphere at 850 hPa and PeKe in the upper troposphere at 250 hPa, to compare composite for the MJO-IO with that for Non-MJO (Fig. 14). In the MJO-IO, strong K’ generation by KmKe is found broadly in the southern Indian Ocean (Fig. 14a), with the highest value found in the central part. Additionally, a secondary peak of KmKe is apparent south of the equator off Sumatra. High KmKe values are also found in the northern Indian Ocean around 5°N and east of Malay Peninsula in the South China Sea. Similar horizontal patterns are also found in the Non-MJO (Fig. 14b), but the maximum in the northern Indian Ocean shifts northeastward, lying north of Sumatra. These distributions of high KmKe generally correspond to the dK’/dt maximum shown in Fig. 11. The KmKe can be decomposed into six terms

$$-\overline{V'_h (V' \cdot \nabla)\overline{V}_h} = -\overline{u'u'}\frac{\partial \overline{u}}{\partial x} - \overline{u'v'}\frac{\partial \overline{u}}{\partial y} - \overline{u'\omega'}\frac{\partial \overline{u}}{\partial p} - \overline{u'v'}\frac{\partial \overline{v}}{\partial x} - \overline{v'v'}\frac{\partial \overline{v}}{\partial y} - \overline{v'\omega'}\frac{\partial \overline{v}}{\partial p}.$$

The dominant contributors to KmKe over the Indian Ocean are the first and second terms on the right hand side (Figs. 15a,b,g,h), which represent barotropic wave accumulation through mean zonal wind convergence (e.g., Webster and Chang 1988; Sobel and Bretherton 1999) and energy conversion through meridional shear of mean zonal winds, respectively. Both terms are associated with a horizontal distribution of mean zonal winds. The $-\overline{u'u'}\partial\bar{u}/\partial x$ term (Figs. 15a,g) dominates the large KmKe values over the northeastern and central south Indian Oceans, corresponding to strong zonal convergence areas of mean westerly winds (Figs. 16a,b). The highest KmKe values found in the southern Indian Ocean are explained as resulting from the $-\overline{u'v'}\partial\bar{u}/\partial y$ term (Figs. 15b,h). The mean westerly winds around the equator drastically changed to the easterlies around 5°S in a north-south direction (Figs. 16a,b). This strong meridional shear of mean zonal winds induces the large K' generation around 5°S if seed disturbances exist. Over the South China Sea, the high KmKe values are attributed to the fifth term (Figs. 15e,k), $-\overline{v'v'}\partial\bar{v}/\partial y$, representing the wave accumulation through mean meridional wind convergence, corresponding to the convergence areas of mean northeasterly winds. However, this energy conversion is largely offset by the first term (Figs. 15a,g) to the east of 105°E, resulting in the KmKe maximum east of the Malay Peninsula.

With respect to PeKe in the upper troposphere during the Non-MJO (Figs. 14d), PeKe has larger values in the southern Indian Ocean than in the northern Indian Ocean although the differences are statistically insignificant. PeKe values during the MJO-IO (Fig. 14c) are generally higher than those during the Non-MJO and statistically significant over broad areas, indicating that synoptic convective activities are high and robust. Higher values of PeKe are located straddling the equator over the eastern Indian Ocean, representing twin convective disturbances across the equator. Since convective activities depend on SST, composite SST for the MJO-IO and Non-MJO are plotted in Fig. 16c and 16d, respectively. Over the area west of Sumatra between 5°S–5°N, SST is broadly high and partly exceeds 28°C, which is sufficient for facilitating active convection, in both composites. This indicates that the difference of PeKe between the two groups cannot be explained by the SST distribution. On the other hand, horizontal convergence of near-surface winds might have a strong impact on convective activities. Since widespread southeasterly winds in the southern Indian Ocean converge around 5°S, synoptic convection can develop easily when seed disturbances are provided by the offshore migration of convection from the western coast of Sumatra. In the northern Indian Ocean, mean northeasterly winds from the South China Sea are much stronger during the MJO-IO compared to those during the Non-MJO, corresponding to drastic SST cooling over the South China Sea. These strong northeasterlies and equatorial westerlies converge over the northeastern Indian Ocean around 5°N, resulting in the convective development during the MJO-IO.

In summary, the eddy kinetic energy budget analysis shows that the K’ generation in the eastern Indian Ocean is apparent when the diurnal cycle over Sumatra is strong. This arises from the barotropic energy conversion from the mean kinetic energy (KmKe) and active synoptic convection (PeKe). The convergence of mean southeasterly winds around 5°S, which provides a favorable condition for development of synoptic disturbances from the seed disturbances excited by the diurnal cycle, is observed in both the MJO-IO and Non-MJO. In contrast, clear differences between the two composites can be seen in the northern hemisphere. In the MJO-IO, strong northeasterly winds blowing into the organized MJO convection cause horizontal convergence in the northeastern Indian Ocean and contribute to the development of the synoptic disturbance there, whereas such features are not observed in the Non-MJO. Resultantly, twin synoptic disturbances straddling the equator are observed only in the MJO-IO.

7. Discussion of the MJO propagation

So far in this study, the development of synoptic disturbances over the eastern Indian Ocean is found when the diurnal cycle over Sumatra is strong. Especially when the MJO convection is located in the Indian Ocean (MJO-IO), the twin cyclonic disturbances straddling the equator develop, implying the enhancement of the Rossby wave response within the MJO. Since the Rossby waves propagate westward, the enhancement of the Rossby wave response may weaken or stop the eastward-propagation of the MJO. This hypothesis is consistent with recent modeling studies indicating that the diurnal cycle tends to hinder the propagation of the MJO across the MC (Hagos et al. 2016; Majda and Yang 2016). From the aspect of moisture budget view point, on the other hand, the intensified

Rossby wave response leads to anomalous drying of the equatorial lower troposphere to the west of the MJO convection through meridional advection, resulting in the facilitation of the eastward-propagation of the MJO (e.g., Maloney 2009). In this section, we will discuss the influence of the diurnal cycle over Sumatra on the MJO propagation.

For this purpose, the MJO events (see the definition in section 2) with active convection over the Indian Ocean (phase 2 and/or 3) during the rainy season are classified into two groups: 30 events in which the strong diurnal events occur and 10 other events. The latter consist of one MJO event in which weak diurnal events occur, and 9 MJO events in which neither strong nor weak diurnal events occur. Note that one event in which both strong and weak diurnal events occur is excluded. Three-quarters of the MJO events occur with strong diurnal events, indicating that the strong diurnal cycle over Sumatra is favorable for the development of the MJO. Table 1 shows the statistics of the MJO events with the strong diurnal events and the others. It shows that the MJO with the strong diurnal cycle has longer duration (30.4 days) compared to the others (24.6 days) on average, but the first and last phases of the MJO are comparable. Average duration in each MJO phase (Table 2) indicates that the phases 2, 3, and 5, corresponding to the MJO path over the Indian Ocean and the western Pacific, contribute to the longer duration for the MJO with the strong diurnal events. These statistics suggest that the strong diurnal cycle over Sumatra contributes to the longer duration of the MJO around the MC. To examine convective activities during the MJO events, time-longitude sections of composite OLR and intraseasonal OLR anomalies averaged for

10°S–10°N for the two MJO groups are shown in Fig. 17. Day 0 indicates the last day of the phase 2 or the first day of the phase 3. Apparent and statistically-significant eastward propagation of intraseasonal convective anomalies across the MC is detected only for the MJO events with the strong diurnal events (Fig. 17, left) whereas intraseasonal convective activities over the Indian Ocean are comparable. In addition, convective activities off the western coast of Sumatra are enhanced rapidly after day 0. For the other MJO events (Fig. 17, right), the intraseasonal convection weakens over the MC. These results indicate that the smooth propagation of the intraseasonal convective anomalies across the MC is accompanied by the strong diurnal events. Interestingly, the intraseasonal convection for the other MJO events develops again over the western Pacific and its signal tends to propagate faster over the MC than that with the strong diurnal cycle, probably due to decoupling with convection over the MC.

It has been known that the behavior of the MJO is distinct between boreal summer and winter. During boreal summer, intraseasonal convection shows not only eastward but also northward propagation, called the boreal summer intraseasonal oscillation (BSISO; e.g., Wang and Rui 1990; Kikuchi et al., 2012; Kiladis et al., 2014). Since this study focuses on the rainy season from September to April, the intraseasonal convection during September–November (SON) may have characteristics of a summer-type MJO compared to that during December–February (DJF). Therefore, we check seasonal dependences of the MJO events (Table 3). Whereas the MJO events with strong diurnal events have weak seasonality, the other MJO events are frequently observed from March to April (MA). Composite OLR and intraseasonal OLR anomalies for the MJO events during SON, DJF, and MA (Fig. 18) shows that the MJO convection with strong diurnal events both during SON and DJF (Fig. 18a, c) shows the smooth eastward propagation over the MC although that over the western Pacific are somewhat stronger during DJF. For the other MJO events during SON (Fig. 18b), the eastward-propagating convection is substantially suppressed over the MC. These results are consistent with those of total composites (Fig. 17). During MA (Fig. 18d, e), on the other hand, convective activities for both the MJO events weaken over the MC and reactivated convection over the western Pacific are stronger for the other MJO events. These results indicate that the influence of the diurnal cycle on the MJO behavior is strong both during SON and DJF but weak during MA. Small differences in the MJO behavior and its dependence on the diurnal events between SON and DJF infer that the difference of the MJO types, i.e., the summer and winter types, does not affect the results of this study. The different relationship between the MJO and the diurnal cycle during MA is left for future work.

The results shown in this paper indicate statistical relationship between the diurnal cycle and the eastward propagation feature of the MJO. However, further studies are needed to clarify the physical mechanism how the diurnal cycle and associated synoptic disturbances over the eastern Indian Ocean affect the MJO propagation, which remains for our future study. The sensitivity experiment by numerical models with and without the diurnal forcing may be one of the promising approaches. In particular, our results indicate that the diurnal cycle only during the MJO phases 2 and 3 affects subsequent behavior of the MJO. Therefore, it seems interesting to enhance or suppress the diurnal forcing in particular MJO phases, in addition to doing so over the whole simulation period irrespective of the phases as done in previous studies such as Hagos et al. (2016).

8. Summary and discussion

In this study, we examine the impact of the diurnal cycle of precipitation over and around Sumatra Island on synoptic disturbances over the eastern Indian Ocean and its relation to the MJO phases and amplitude. A sequence of days when the diurnal cycle of precipitation over the Sumatra area are strong (weak) is defined as a strong (weak) diurnal event. Much higher precipitation amounts around the western coast of Sumatra are confirmed during the strong diurnal events, indicating that the strong diurnal cycle provides large condensation heating. The strong diurnal events are found most frequently in October and November, generally corresponding to the peak rainy season (e.g., Hamada et al. 2002). In addition to the seasonal dependency, the strong diurnal events preferentially occur during the MJO phases 2 and 3 when the MJO convection lies over the Indian Ocean, consistent with previous analysis (e.g., Fujita et al. 2011; Peatmann et al. 2014). We also confirm the nighttime offshore migration of precipitation (e.g., Mori et al. 2004) reaching 500 km off the coast, located in the open ocean, when the strong diurnal events occur.

Although the modulation of the diurnal cycle by the MJO has been studied intensively in recent years (e.g., Tian et al. 2006; Ichikawa and Yasunari 2007; Rauniyar and Walsh 2011; Fujita et al. 2011; Peatman et al. 2014), the upscale effects of the diurnal cycle on synoptic and intraseasonal disturbances remain elusive. Therefore, we examine the activities of synoptic disturbances over the eastern Indian Ocean by the eddy kinetic energy budget analysis based on the diurnal events considering the MJO phases and amplitude. The K’ generation in the southeastern Indian Ocean is apparent when the diurnal cycle over Sumatra is strong regardless of the MJO phases and amplitude. It is related to the development of synoptic disturbances from the seed disturbances arising from the diurnal cycle by virtue of the favorable mean state such as the convergence of mean southeasterly winds around 5°S. In contrast, synoptic disturbances in the northern Indian Ocean off Sumatra develop only in the MJO-IO, which can result from convergence of the mean equatorial westerly winds over the Indian Ocean and the mean northeasterly winds from the South China Sea blowing into the convective center of the MJO in the Indian Ocean. Note that the intensified northeasterly winds are likely associated with strong cold surges over the South China Sea that are known to be observed frequently when the MJO convection is located over the Indian Ocean or the MC (Jeong et al. 2005 and Chang et al. 2005). As a result, the twin disturbances straddle the equator and migrate poleward and/or westward rapidly only during the MJO-IO, suggesting that the Rossby wave response within the MJO is intensified. In the Non-MJO, on the other hand, the synoptic disturbances develop mainly over the southern Indian Ocean and do not migrate in any direction. This indicates that although the strong diurnal cycle over Sumatra trigger the synoptic disturbances over the eastern Indian Ocean regardless of the MJO phase and existence, the twin cyclonic disturbances across the equator can develop only when the MJO convection is located over the Indian Ocean. When the diurnal cycle is weak over Sumatra, the K’ decrease is found over the eastern Indian Ocean, showing the suppression of the synoptic disturbances.

To examine impact of the diurnal cycle on the MJO behavior, a comparison of the MJO events having the phase 2 and/or 3 with the strong diurnal events with such MJO events but without the strong diurnal events is presented. The MJO events with the strong diurnal events tend to have longer duration and stronger convective activities around the MC compared to the other MJO events, indicating that the strong diurnal cycle of precipitation over Sumatra facilitates the smooth propagation of the intraseasonal convection across the MC. For the MJO events without the strong diurnal events, whereas the intraseasonal convective anomalies weaken over the MC, the overall MJO signals tend to propagate across the MC faster than the MJO events with the strong diurnal events, and the intraseasonal convection strengthens again over the western Pacific. Note that the MJO propagation speed may be important for forecasting when teleconnection patterns are excited by the MJO convection over the western Pacific, which cause significant impacts even in the mid-latitudes (e.g., Zhang 2013).

Whereas an averaged MJO event has been known to propagate eastward with a mean speed of ~5 ms^{-1} over the Ind-Pacific warm pool (e.g., Zhang 2005), the behavior of individual MJO events such as the amplitude and propagation speed differs considerably from event to event (e.g., Kerns and Chen 2016; Wang et al. 2019). The presence or absence of the strong diurnal events focused in this study may play a role in understanding the MJO diversity. In addition, only one MJO index (the RMM index) is used to identify the MJO events and to determine its amplitude and phases in this study. The statistics of the MJO events in Table 1-3 may have sensitivity to the MJO indices (Kiladis et al. 2014).

In this study, strong and weak diurnal events are identified first. The factors determining the amplitude of the diurnal cycle remain unclear. The diurnal cycle in the tropics is primarily driven by insolation. However, the number of the strong diurnal events in the equinox months (September and March) are smaller than that in October and November (Fig. 2). The favorable MJO phases for the diurnal cycle (the phases 2 and 3) correspond to the convective suppressed condition over the MC, linked to high insolation (Fig. 10 and previous studies). However, the suppressed phases are also observed in the rear side of the MJO convection (i.e., the phases 6 and 7). Another factor such as moisture condition may influence on the diurnal cycle of precipitation. From large-scale viewpoint, ENSO might be the factor. The strong diurnal events identified in this study are classified into El Niño (2002, 2004, 2006, and 2009), La Niña (2000, 2005, 2007, 2008, 2010, and 2011), and neutral years (2001, 2003, 2012, and 2013) based on the ENSO index derived by NOAA. There are no clear differences among the numbers of the strong diurnal events per year during the El Niño (9), La Niña (13), and neutral years (10). This is consistent with previous studies (e.g., Rauniyar and Walsh 2013) indicating that dependency of the strength of the diurnal cycle on ENSO has regional differences due to topography. There are multiple factors influencing the strength of the diurnal cycle such as insolation, moisture condition, topography, and others. Further studies are needed to detect all factors and estimate their contribution rate.

Our results show the impact of the strong diurnal events over Sumatra on the development of the synoptic disturbances over the eastern Indian Ocean. However, the importance of diurnal fluctuations or migration of precipitation still remains unclear. The composite analysis based on the strong diurnal cycle of precipitation over Sumatra also shows a high amount of daily-mean precipitation simultaneously. Therefore, it is uncertain whether diurnal or sustained heat release by precipitation off the coast has a large effect on triggering synoptic disturbances over the Indian Ocean, which possibly link to the MJO propagation. To clarify the aforementioned question, we might have to focus on mesoscale convective systems to understand how diurnal convection near the coast leads to the synoptic disturbances in the open ocean. However, the time and horizontal resolutions of the reanalysis data are too coarse, and the intensive observations have covered a limited area. Sensitivity experiments by numerical models might be useful but there are few models that can reproduce multiscale phenomena including the diurnal offshore migration, synoptic disturbances, and the MJO. Recently, the global cloud resolving models have been developed internationally. For example, Miura et al. (2007) have simulated the MJO successfully using the global cloud-resolving Nonhydrostatic ICosahedral Atmospheric Model (NICAM; Tomita and Satoh 2004).

The analysis focusing on the offshore regions using these high-resolution cloud resolving models might be useful for future works.

Acknowledgments

The authors would like to thank Kunio Yoneyama for helpful discussion. Comments from two anonymous reviewers also improved the original manuscript. This study is partly supported by Grants-in-Aid for Scientific Research (18H05879 and 20H02252) of the Japan Society for the Promotion of Science.

References

Albright et al. 1985 Albright, M. D., E. E. Recker, R. J. Reed, and R. Dang, 1985: The diurnal variation of deep convection and inferred precipitation in the central tropical Pacific during January–February 1979. *Mon. Wea. Rev.*, **113**, 1663–1680.

Aonashi, A., J. Awaka, M. Hirose, T. Kozu, T. Kubota, G. Liu, S. Shige, S., Kida, S. Seto, N.Takahashi, and Y. N. Takayabu, 2009: GSMaP passive, microwave precipitation retrieval algorithm: Algorithm description and validation. *J. Meteor. Soc. Japan*, **87A**, 119–136.

Birch, C. E., S. Webster, S. C. Peatman, D. J. Parker, A. J. Matthews, Y. Li, and M. E. E. Hassim, 2016: Scale interactions between the MJO and the western Maritime Continent. *J. Climate*, **29**, 2471–2492.

Chang, C.-P., P. A. Harr, H.-J. Chen, 2005: Synoptic disturbances over the equatorial South China Sea and Western Maritime Continent during boreal winter. *Mon. Wea. Rev.*, **133**, 489–503.

Fujita, M., K. Yoneyama, S. Mori, and T. Nasuno, 2011: Diurnal convection peaks over the eastern Indian Ocean off Sumatra during different MJO phases. *J. Meteor. Soc. Japan*, **89A**, 317–330.

Gray, W. M., and R. W. Jacobson Jr., 1977: Diurnal variation of deep cumulus convection. *Mon. Wea. Rev*., **105**, 1171–1188.

Hamada, J.-I., M. D. Yamanaka, J. Matsumoto, S. Fukao, P. A. Winarso, and T. Sribimawati, 2002: Spatial and temporal variations of the rainy season over Indonesia and their link to ENSO. *J. Meteor. Soc. Japan*, **80**, 285–310.

Hagos, S. M., C. Zhang, Z. Feng, C. D. Burleyson, C. De Mott, B. Kerns, J. J. Benedict, and M. N. Martini, 2016: The impact of the diurnal cycle on the propagation ofMadden–Julian oscillation convection across the Maritime Continent. *J. Adv. Model. Earth Syst.*, **8**, 1552–1564.

Houze, R. A., Jr., S. G. Geotis, F. D. Marks, and A. K. West, 1981: Winter monsoon convection in the vicinity of North Borneo. Part I: Structure and time variation of the clouds and precipitation. *Mon. Wea. Rev.*, **109**, 1595–1614.

Ichikawa, H., and T. Yasunari, 2006: Time–space characteristics of diurnal rainfall over Borneo and surrounding oceans as observed by TRMM-PR. *J. Climate*, **19**, 1238–1260.

Ichikawa, H., and T. Yasunari, 2007: Propagating diurnal disturbances embedded in the Madden–Julian Oscillation. *Geophys. Res. Lett.*, **34**, L18811.

Inness, P. M., and J. M. Slingo, 2006: The interaction of the Madden–Julian oscillation with the Maritime Continent in a GCM. *Quart. J. Roy. Meteor. Soc.*, **132**, 1645–1667.

Jeong, J.-H., C.-H. Ho, B.-M. Kim, W.-T. Kwon, 2005: Influence of the Madden-Julian Oscillation on wintertime surface air temperature and cold surges in east Asia. *J. Geophys. Res.*, **110**, D11104.

Kerns, B. W., and S. S. Chen, 2016: Large-scale precipitation tracking and the MJO over the Maritime Continent and Indo-Pacific warm pool. *J. Geophys. Res.*, **121**, 8755-8776.

Kim, D., K, and Coauthors, 2009: Application of MJO simulation diagnostics to climate models. *J. Climate*, **22**, 6413–6436.

Kim, D., H. Kim, and M.-I. Lee, 2017: Why does the MJO detour the Maritime Continent during austral summer? *Geophys. Res. Lett.*, **44**, 2579–2587.

Kikuchi, K., and B. Wang, 2008: Diurnal precipitation regimes in the global tropics. *J. Climate*, **21**, 2680–2696.

Kikuchi, K., B. Wang, and Y. Kajikawa, 2012: Bimodal representation of the tropical intraseasonal oscillation. *Clim. Dyn.*, **38**, 1989–2000.

Kiladis, G. N., J. Dias, K. H. Straub, M. C. Wheeler, S. N. Tulich, K. Kikuchi, K. M. Weickmann, and M. J. Ventrice, 2014: A comparison of olr and circulation-based indices for tracking the MJO. *Mon. Wea. Rev.*, **142**, 1697–1715.

Kobayashi, S., Y. Ota, Y. Harada, A. Ebita, M. Moriya, H. Onoda, K. Onogi, H. Kamahori, C. Kobayashi, H. Endo, K. Miyaoka, and K. Takahashi, 2015: The JRA-55 Reanalysis:

General Specifications and Basic Characteristics. *J. Meteor. Soc. Japan*, **93**, 5-48.

Kubota, T., and Coauthors, 2007: Global Precipitation Map using Satelliteborne Microwave Radiometers by the GSMaP Project : Production and Validation, *IEEE Trans. Geosci. Remote Sens.*, **45**, No. 7, 2259–2275.

Kubota, T., and Coauthors, 2020: Global Satellite Mapping of Precipitation (GSMaP) products in the GPM era, Satellite precipitation measurement, Springer, pp355-373.

Lau, K.-H., and N.-C. Lau, 1992: The Energetics and Propagation Dynamics of Tropical Summertime Synoptic-Scale Disturbances. *Mon. Wea. Rev.*, **120**, 2523–2539.

Liebmann, B., and C. A. Smith, 1996: Description of a complete (interpolated), outgoing longwave radiation dataset. *Bull. Amer. Meteor. Soc.*, **77**, 1275–1277.

Love, B. S., A. J. Matthews, and G. M. S. Lister, 2011: The diurnal cycle of precipitation over the Maritime Continent in a highresolution atmospheric model. *Quart. J. Roy. Meteor. Soc.*, **137**, 934–947, doi:10.1002/qj.809.

Madden, R., 1986: Seasonal variations of the 40-50 day oscillation in the tropics. *J. Atmos. Sci.*, **43**, 3138–3158.

Madden, R. A. and P. R. Julian, 1971: Detection of a 40-50-Day Oscillation in the Zonal Wind in the Tropical Pacific. *J. Atmos. Sci.*, **28**, 702-708.

Madden, R. A. and P. R. Julian, 1972: Description of Global-Scale Circulation Cells in the Tropics with a 40-50-Day period. *J. Atmos. Sci.*, **29**, 1109-1123.

Madden, R. A., and P. R. Julian, 1994: Observations of the 40-50-Day Tropical Oscillation

— A Review. *Mon. Wea. Rev.*, **122**, 814–837.

Majda, A. J., and Q. Yang, 2016: A multiscale model for the intraseasonal impact of the diurnal cycle over the Maritime Continent on the Madden–Julian oscillation. *J. Atmos. Sci.*, **73**, 579–604.

Maloney, E. D., 2009: The moist static energy budget of a composite tropical intraseasonal oscillation in a climate model. *J. Climate*, **22**, 711–729.

Maloney, E. D., and M. J. Dickinson, 2003: The Intraseasonal Oscillation and the Energetics of Summertime Tropical Western North Pacific Synoptic-Scale Disturbances. *J. Atmos. Sci.*, **60**, 2153–2168.

Mapes, B. E., T. T. Warner, M. Xu, 2003: Diurnal patterns of rainfall in northwestern South America. Part III: Diurnal gravity waves and nocturnal convection offshore. *Mon. Wea. Rev.*, **131**, 830–844.

Matthews, A. J., 2008: Primary and successive events in the Madden–Julian oscillation. *Quart. J. Roy. Meteor. Soc.*, **134**, 439–453.

Mori, S., and Coauthors, 2004: Diurnal land–sea rainfall peak migration over Sumatera Island, Indonesian Maritime Continent observed by TRMM satellite and intensive rawinsonde soundings. *Mon. Wea. Rev.*, **132**, 2021–2039.

Murakami, M., 1983: Analysis of the deep convective activity over the western Pacific and southwest Asia. Part I: Diurnal variation. *J. Meteor. Soc. Japan*, **61**, 60–76.

Nakazawa, T., 1988: Tropical Super Clusters within Intraseasonal Variations over the

Western Pacific. *J. Meteor. Soc. Japan*, **66**, 823–839.

Neale, R., and J. Slingo, 2003: The Maritime Continent and its role in the global climate: A GCM study. *J. Climate*, **16**, 834–848.

Nesbitt, S. W., and E. J. Zipser, 2003: The diurnal cycle of rainfall and convective intensity according to three years of TRMM measurements. *J. Climate*, **16**, 1456–1475.

Nitta, T., 1972: Energy Budget of Wave Disturbances over the Marshall Islands during the Years of 1956 and 1958. *J. Meteor. Soc. Japan*, **50**, 71-84.

Nitta, T., and S. Sekine, 1994: Diurnal variation of convective activity over the tropical western Pacific. *J. Meteor. Soc. Japan*, **72**, 627–641.

Ogino, S., M. D. Yamanaka, S. Mori, and J. Matsumoto, 2016: How much is the precipitation amount over the tropical coastal region? *J. Climate*, **29**, 1231–1236.

Peatman, S. C., A. J. Matthews, and D. P. Stevens, 2014: Propagation of the Madden-Julian Oscillation through the Maritime Continent and scale interaction with the diurnal cycle of precipitation. *Quart. J. Roy. Meteor. Soc.*, **140**, 814–825.

Qian, J.-H., A. W. Robertson, and V. Moron, 2010: Interactions among ENSO, the monsoon, and diurnal cycle in rainfall variability over Java, Indonesia. *J. Atmos. Sci.*, **67**, 3509–3524.

Qian, J.-H., A. W. Robertson, and V. Moron, 2013: Diurnal cycle in different weather regimes and rainfall variability over Borneo associated with ENSO. *J. Climate*, **26**, 1772–1790.

Ramage, C. S., 1968: Role of a tropical “maritime continent” in the atmospheric circulation. *Mon. Wea. Rev.*, **96**, 365–370.

Rauniyar, S. P., and K. J. E. Walsh, 2011: Scale interaction of the diurnal cycle of rainfall over the MC and Australia: Influence of the MJO. *J. Climate*, **24**, 325–348.

Rauniyar, S. P., and K. J. E. Walsh, 2013: Influence of ENSO on the diurnal cycle of rainfall over the Maritime Continent and Australia. *J. Climate*, **26**, 1304–1321.

Reynolds, R. W., T. M. Smith, C. Liu, D. B. Chelton, K. S. Casey, and M. G. Scchlax, 2007: Daily high-resolution-blended analysis for sea surface temperature. *J. Climate*, **20**, 5473–5496.

Sakurai, N., and Coauthors, 2005: Diurnal cycle of cloud system migration over Sumatera Island. *J. Meteor. Soc. Japan*, **83**, 835–850.

Seiki, A., and Y. N. Takayabu, 2007: Westerly wind bursts and their relationship with intraseasonal variations and ENSO. Part II: Energetics over the western and central Pacific. *Mon. Wea. Rev.*, **133**, 3346–3361.

Seiki, A., Y. N. Takayabu, T. Hasegawa, and K. Yoneyama, 2018: Lack of westerly wind bursts in unmaterialized El Niño years. *J. Climate*, **31**, 593–612.

Seo, K.-H., W. Wang, J. Gottschalck, Q. Zhang, J.-K. E. Schemm, W. R. Higgins, andA. Kumar, 2009: Evaluation of MJO forecast skill from several statistical and dynamical forecast models. *J. Climate*, **22**, 2372–2388.

Sobel, A. H., and C. S. Bretherton, 1999: Development of Synoptic-Scale Disturbances over the Summertime Tropical Northwest Pacific. *J. Atmos. Sci.*, **56**, 3106–3127.

Takayabu, Y. N., 2002: Spectral representation of rain profiles and diurnal variations observed with TRMM PR over the equatorial area. *Geophys. Res. Lett.*, **29**, 1584.

Tian, B., D. E. Waliser, and E. J. Fetzer, 2006: Modulation of the diurnal cycle of tropical deep convective clouds by the MJO. *Geophys. Res. Lett.*, **33**, L20704.

Tomita, H., and M. Satoh, 2004: A new dynamical framework of nonhydrostatic global model using the icosahedral grid, *Fluid Dyn. Res.*, **34**, 357–400.

Vitart, F., and F. Molteni, 2010: Simulation of the Madden–Julian oscillation and its teleconnections in the ECMWF forecast system. *Quart. J. Roy. Meteor. Soc.*, **136**, 842–855.

Wang, B., G. S. Chen, and F. Liu, 2019: Diversity of the Madden-Julian Oscillation. *Science Advances*, **5**.

Wang, B., and H. Rui, 1990: Synoptic climatology of transient tropical intraseasonal convection anomalies: 1975-1985. *Meteor. Atmos. Phys.*, **44**, 43–61.

Webster, P. J., and H. R. Chang, 1988: Equatorial energy accumulation and emanation regions: Impacts of a zonally varying basic state. *J. Atmos. Sci.,* **45**, 803–829.

Wheeler, M., and H. H. Hendon, 2004: An all-season real-time multivariate MJO index: Development of an index for monitoring and prediction. *Mon. Wea. Rev.*, **132**, 1917–1932.

Wu, C. H., and H. H. Hsu, 2009: Topographic influence on the MJO in the Maritime Continent. *J. Climate*, **22**, 5433–5448.

Yamanaka, M. D., 2016: Physical climatology of Indonesian Maritime Continent: An outline to comprehend observational studies. *Atmos. Res.*, **178-179**, 231-259.

Yang, G.-Y., and J. Slingo, 2001: The diurnal cycle in the Tropics. *Mon. Wea. Rev.*, **129**, 784–801.

Yokoi, S., and coauthors, 2017: Diurnal cycle of precipitation observed in the western coastal area of Sumatra Island: Offshore preconditioning by gravity waves. *Mon. Wea. Rev.*, **145**, 3745–3761.

Yokoi, S., S. Mori, F. Syamsudin, U. Haryoko, and B. Geng, 2019: Environmental conditions for nighttime offshore migration of precipitation area as revealed by in situ observation off Sumatra Island. *Mon. Wea. Rev.*, **147**, 3391-3407.

Zhang, C., 2005: Madden-Julian Oscillation. *Rev. of Geophys.*, **43**, doi:10.1029/2004RG000158.

Zhang, C., and M. Dong, 2004: Seasonality in the Madden–Julian Oscillation. *J. Climate*, **17**, 3169–3180.

Zhang, C., 2013: Madden-Julian Oscillation: Bridging weather and climate. *Bull. Amer. Meteor. Soc.*, **94**, 1849–1870.

Zhang, C., and J. Ling, 2017: Barrier effect of the Indo-Pacific Maritime Continent on the MJO: Perspectives from tracking MJO precipitation. *J. Climate*, **30**, 3439–3459.

List of Figures

Fig. 1 (upper) Amplitude of the diurnal harmonic A of precipitation rate (mm day^{-1}) averaged over the study period, and (lower) the local time of maximum precipitation of the mean diurnal cycle (t_0). The black box represents the Sumatra area (95°E–105°E, 5°S–5°N).

Fig. 2 Monthly distributions of the number (black bars) and accumulated days (gray bars) of the strong diurnal events on the left ordinate. The solid line indicates monthly mean precipitation amount (mm day^{-1}) averaged for the Sumatra area on the right ordinate, while the dashed line represents the ratio of precipitation amount during the strong diurnal events to the total monthly precipitation amount on the left ordinate. Dotted line shows mean amplitude of the diurnal events multiplied by ten on the right ordinate.

Fig. 3 Composite daily-mean precipitation (mm day^{-1}) for (left) the strong and (right) weak diurnal events averaged between day −1 and day +1. Dotted area represents more than the 95% confidence level. Lower panels indicate time evolution of diurnal precipitation averaged for the Sumatra area. The abscissa represents the time lag in days from the reference day (i.e., day 0).

Fig. 4 Composite diurnal cycle of hourly precipitation (mm day^{-1}) for the strong diurnal events on day 0. Dotted area represents more than the 95% confidence level. The white line indicates the coastline used for Fig. 5.

Fig. 5 Composite diurnal cycle of hourly precipitation (mm day^{-1}) for the strong diurnal events on day 0 as a function of distance from the coastline. Enclosed dotted areas represent more than the 95% confidence level. Note that the diurnal cycle is depicted from 12LT to 18LT the following day for 30 hours to represent one cycle clearly.

Fig. 6 The composites for (left) K’ (m^2s^{-2}) and (right) tendency of K’ (dK’/dt) (10^{-5} m^2s^{-3}) at 850 hPa for the strong diurnal events. Dotted areas represent more than the 95% confidence level. The numbers on the top right sides show lags in days from the reference day (i.e., day 0).

Fig. 7 composite eddy relative vorticity at 850 hPa (10^{-5} s^{-1}) averaged from day 0 to day +2 for the strong diurnal events. Dotted areas represent more than the 95% confidence level. Red (blue) shading in the northern (southern) hemisphere represents cyclonic eddies.

Fig. 8 Time-longitude sections of composite dK’/dt at 850 hPa (10^{-5} m^2s^{-3}) for (left) the strong and (right) weak diurnal events averaged for (upper) 3°N–13°N and (lower) 3°S–13°S. Gray contours indicate more than the 95% confidence level.

Fig. 9 Differences of composite dK’/dt at 850 hPa between the strong and weak diurnal events. Positive values represent larger dK’/dt for the strong diurnal events. Contours indicate more than the 95% confidence level using the two-sample Student’s t test.

Fig. 10 (left) Accumulated days for the strong diurnal events in each MJO phase. Black bars indicate the days when the MJO amplitude exceeds 1.0, and gray bars represent the days during the MJO events defined in this study when the MJO amplitude exceeds 1.0 for consecutive 15 days. The “Non” refers to the MJO inactive days (see Section 2). (right)

Total number of days for each MJO phase when the MJO amplitude exceeds 1.0 during the rainy season.

Fig. 11 The composite dK'/dt at 850 hPa (10^{-5} m^{2}s^{-3}) for the strong diurnal events during (left) the MJO-IO and (right) Non-MJO. Dotted areas represent more than the 95% confidence level. Thick black lines show 20–100 days bandpass-filtered OLR of −20 Wm^{-2}. The numbers on the top right sides show lags in days from the reference day (i.e., day 0).

Fig. 12 Same as Fig. 8 except for the strong diurnal events during (left) the MJO-IO and (right) Non-MJO. Thick black lines show negative values of 20–100 days bandpass-filtered OLR with intervals of 5.0 Wm^{-2}.

Fig. 13 Composite vertical structures of each term (10^{-5} m^2 s^{-3}) in (a) the eddy kinetic energy budget and (b) Student's t statistics from 1000 to 150 hPa for all the strong diurnal events on day 0 averaged over the southeastern Indian ocean (1.25–6.25S, 92.5–102.5E). The dark gray line in (b) indicates the 95% confidence level.

Fig. 14 (a, b) Composite KmKe at 850 hPa (10^{-5} m^2 s^{-3}) and (c, d) PeKe at 250 hPa (10^{-5} m^2 s^{-3}) for the strong diurnal events during (a, c) the MJO-IO and (b, d) Non-MJO on day 0. Dotted areas represent more than the 95% confidence level.

Fig. 15 Composites of each term composing KmKe at 850 hPa (10^{-5} m^2 s^{-3}) for the strong diurnal events during (a-f) the MJO-IO and (g-l) Non-MJO on day 0. Dotted areas represent more than the 95% confidence level.

Fig. 16 (a, b) Composite mean zonal winds at 850 hPa (m s^{-1}) and (c, d) SST (°C) for the strong diurnal events during (a, c) the MJO-IO and (b, d) Non-MJO on day 0. Dotted areas represent more than the 95% confidence level. The vectors indicate the composite mean wind fields at (a, b) 850 hPa and (c, d) 1000 hPa, where either the zonal or the meridional component is significant at the 95% level.

Fig. 17 Time-longitude sections of composite equatorial OLR (shading) and 20–100 days bandpass-filtered OLR (contours) averaged between 10°S and 10°N for (left) the MJO events with the strong diurnal events and (right) the other MJO events. All MJO events have phase 2 and/or 3. Solid (dashed) contours indicate negative (positive) values with intervals of 5.0 Wm^{-2}. Day 0 indicates the last day of the phase 2 or the first day of the phase 3. Dotted areas represent more than the 95% confidence level of composite bandpass-filtered OLR.

Fig. 18 Same as Fig. 17 except for the MJO events during (a, b) SON, (c) DJF, and (d, e) MA on day 0. Note that composites for the other MJO events during DJF are not shown due to only one sample.

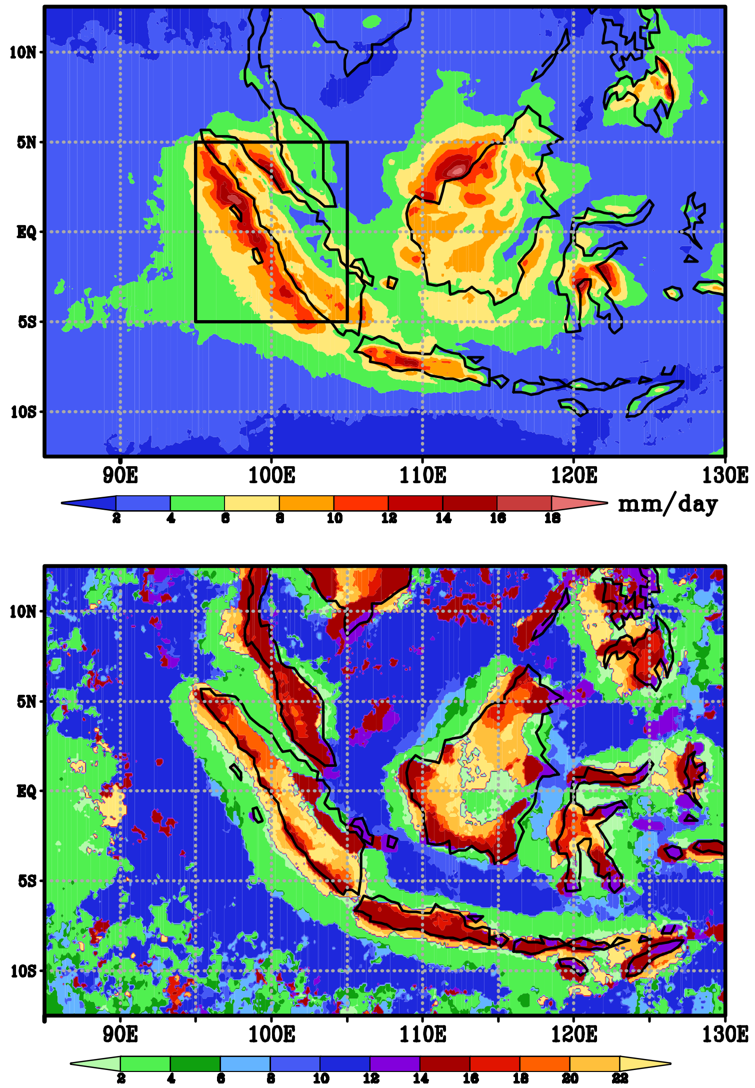

Fig. 1 (upper) Amplitude of the diurnal harmonic A of precipitation rate (mm day^{-1}) averaged over the study period, and (lower) the local time of maximum precipitation of the mean diurnal cycle (t_0). The black box represents the Sumatra area (95°E–105°E, 5°S–5°N).

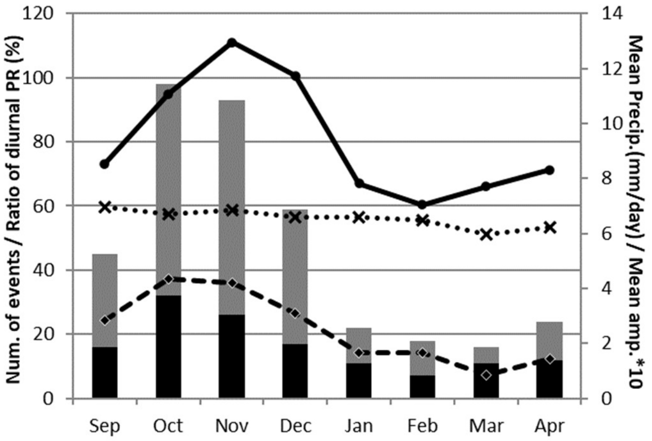

Fig. 2 Monthly distributions of the number (black bars) and accumulated days (gray bars) of the strong diurnal events on the left ordinate. The solid line indicates monthly mean precipitation amount (mm day^{-1}) averaged for the Sumatra area on the right ordinate, while the dashed line represents the ratio of precipitation amount during the strong diurnal events to the total monthly precipitation amount on the left ordinate. Dotted line shows mean amplitude of the diurnal events multiplied by ten on the right ordinate.

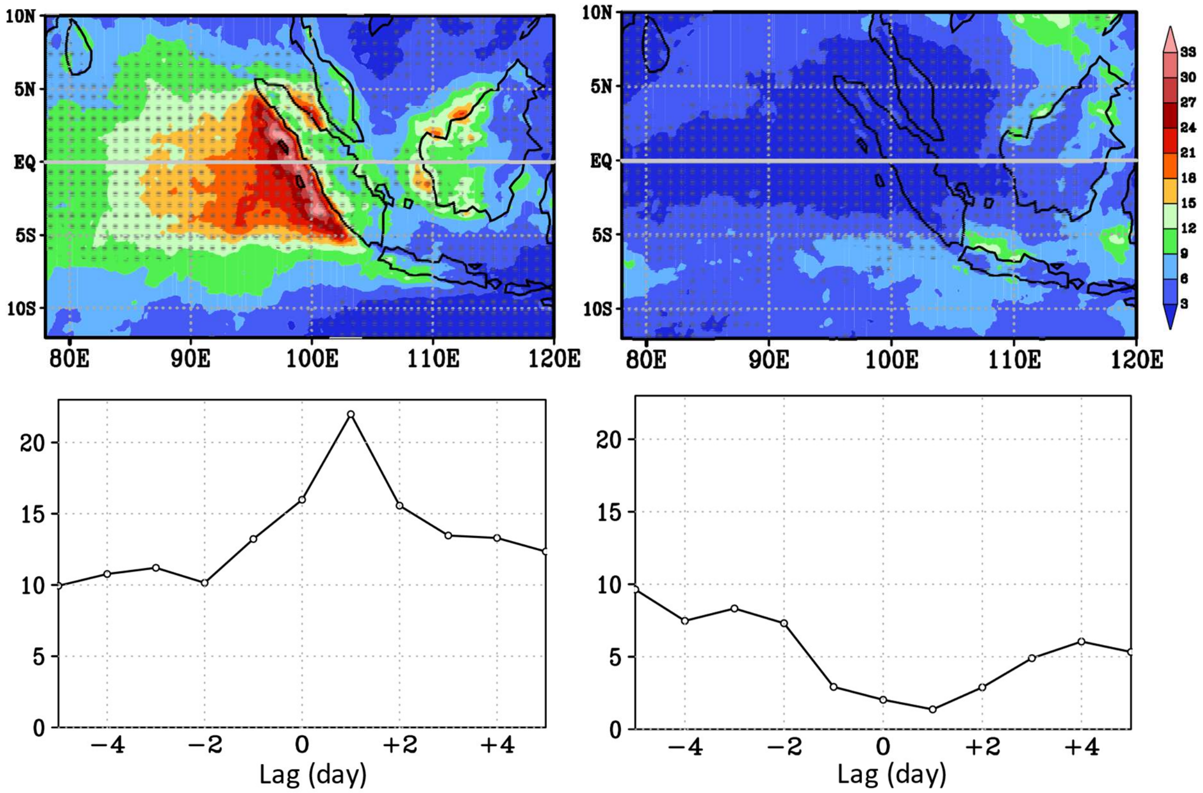

Fig. 3 Composite daily-mean precipitation (mm day^{-1}) for (left) the strong and (right) weak diurnal events averaged between day −1 and day +1. Dotted area represents more than the 95% confidence level. Lower panels indicate time evolution of diurnal precipitation averaged for the Sumatra area. The abscissa represents the time lag in days from the reference day (i.e., day 0).

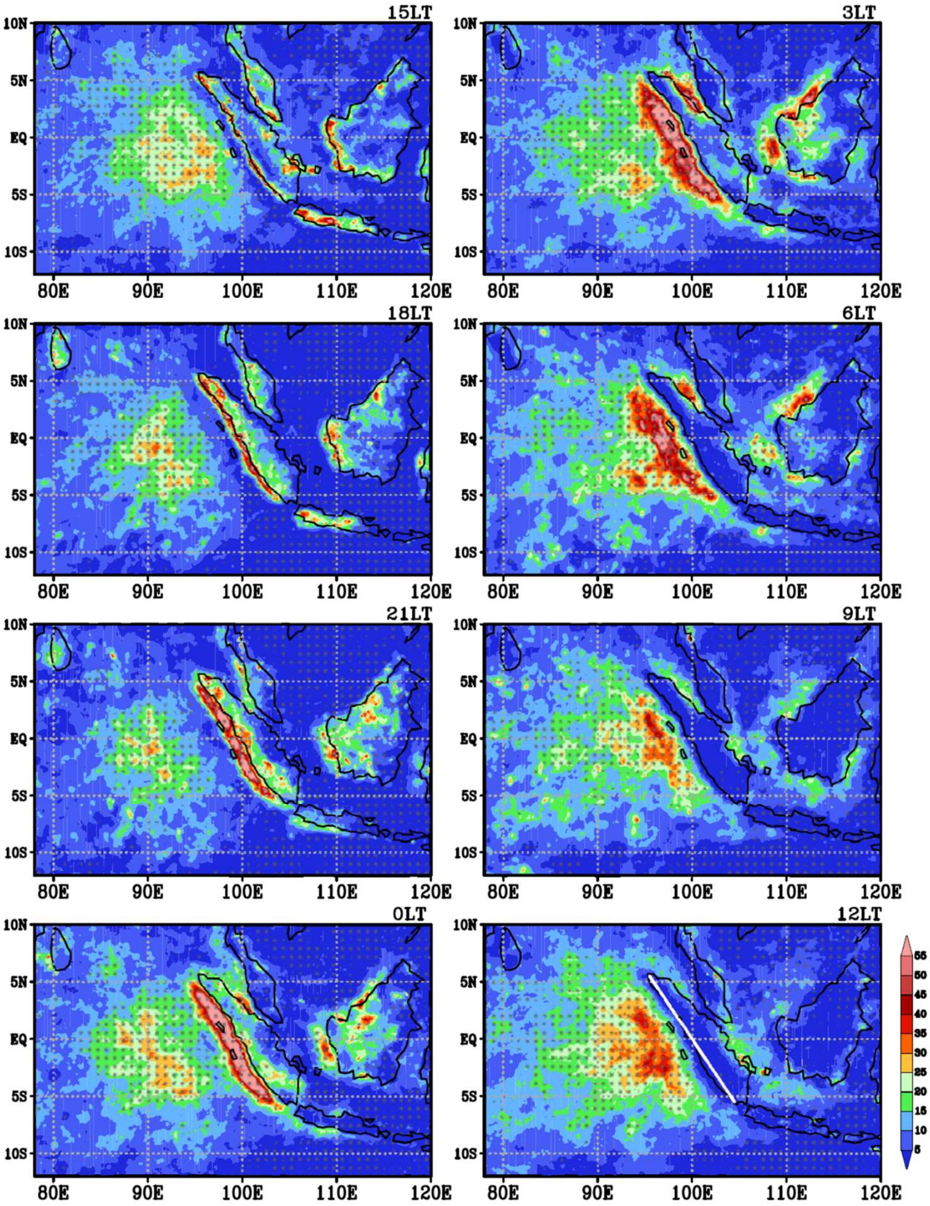

Fig. 4 Composite diurnal cycle of hourly precipitation (mm day^{-1}) for the strong diurnal events on day 0. Dotted area represents more than the 95% confidence level. The white line indicates the coastline used for Fig. 5.

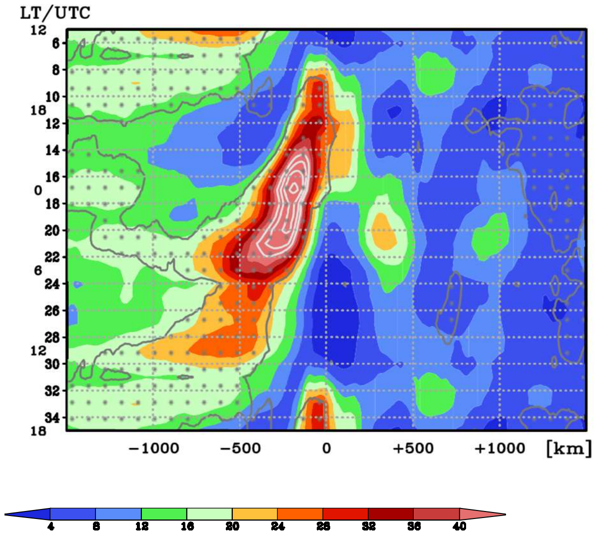

Fig. 5 Composite diurnal cycle of hourly precipitation (mm day^{-1}) for the strong diurnal events on day 0 as a function of distance from the coastline. Enclosed dotted areas represent more than the 95% confidence level. Note that the diurnal cycle is depicted from 12LT to 18LT the following day for 30 hours to represent one cycle clearly.

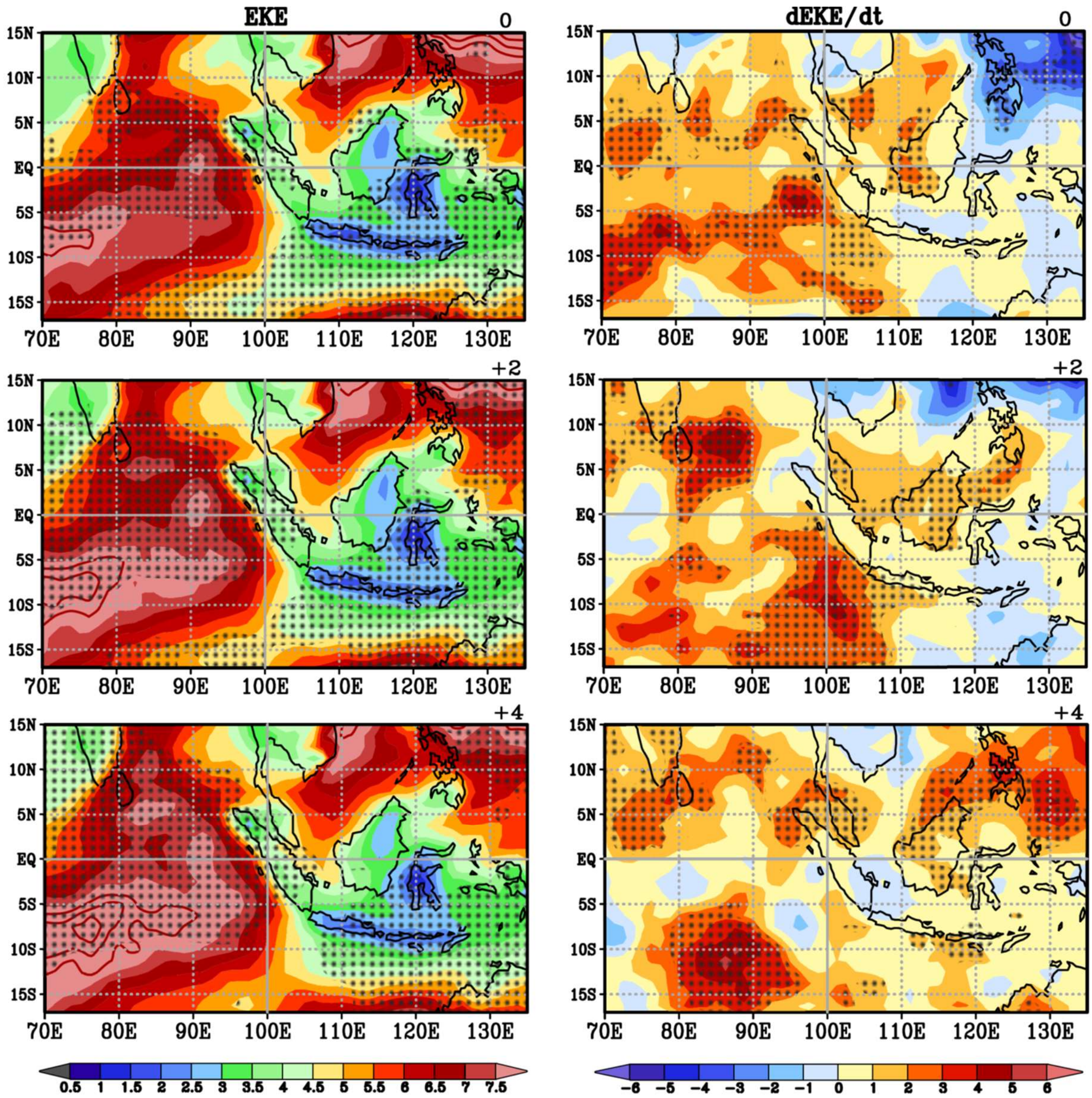

Fig. 6 The composites for (left) K' (m^{2}s^{-2}) and (right) tendency of K' (dK'/dt) (10^{-5} m^{2}s^{-3}) at 850 hPa for the strong diurnal events. Dotted areas represent more than the 95% confidence level. The numbers on the top right sides show lags in days from the reference day (i.e., day 0).

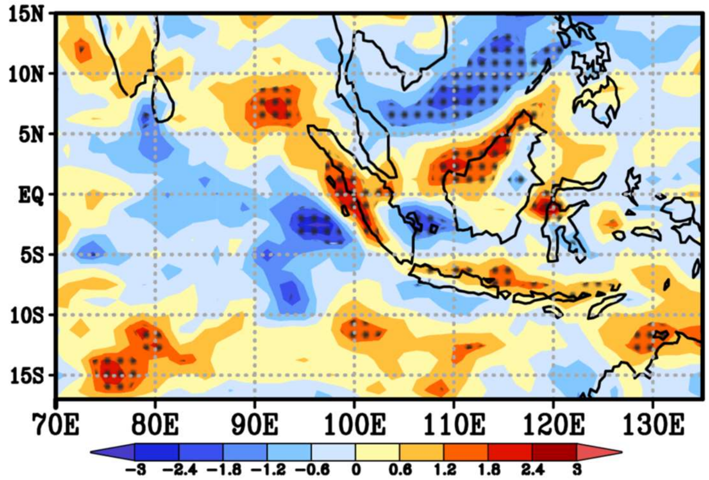

Fig. 7 composite eddy relative vorticity at 850 hPa (10^{-5} s^{-1}) averaged from day 0 to day +2 for the strong diurnal events. Dotted areas represent more than the 95% confidence level. Red (blue) shading in the northern (southern) hemisphere represents cyclonic eddies.

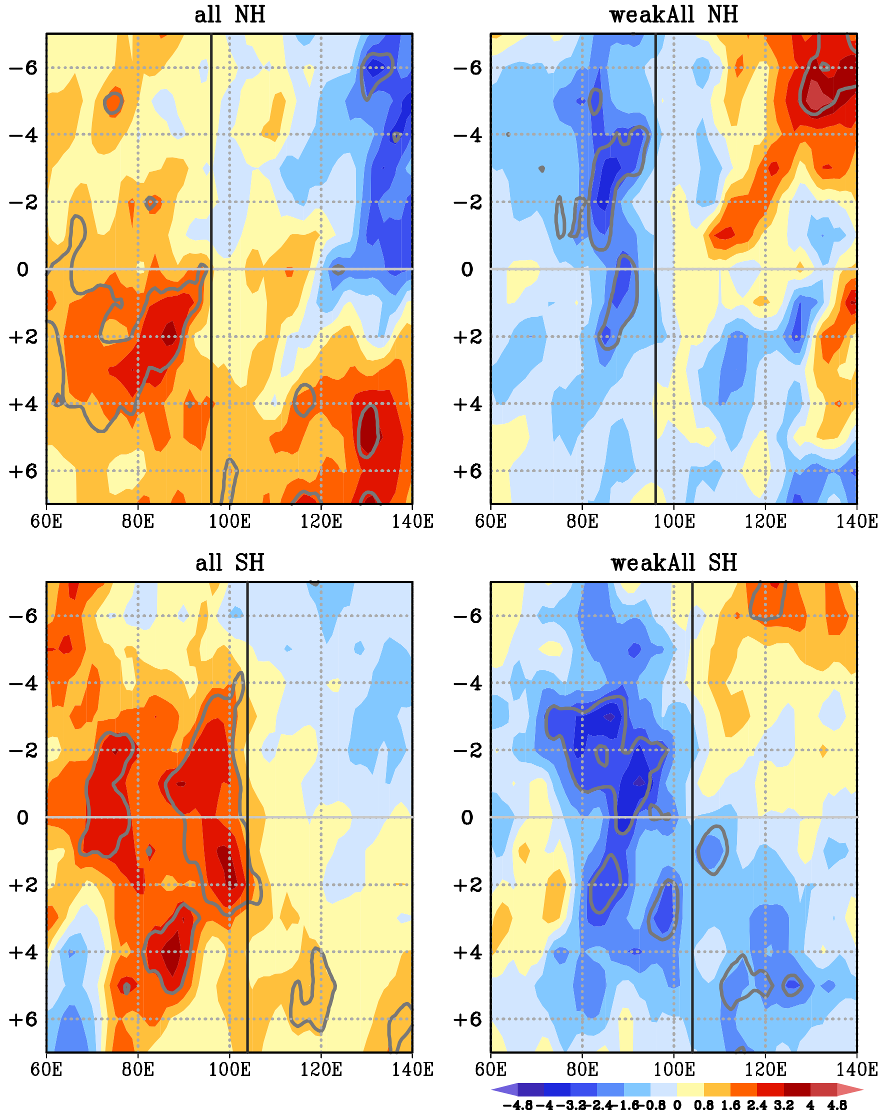

Fig. 8 Time-longitude sections of composite dK'/dt at 850 hPa (10^{-5} m^2s^{-3}) for (left) the strong and (right) weak diurnal events averaged for (upper) 3°N–13°N and (lower) 3°S–13°S. Gray contours indicate more than the 95% confidence level.

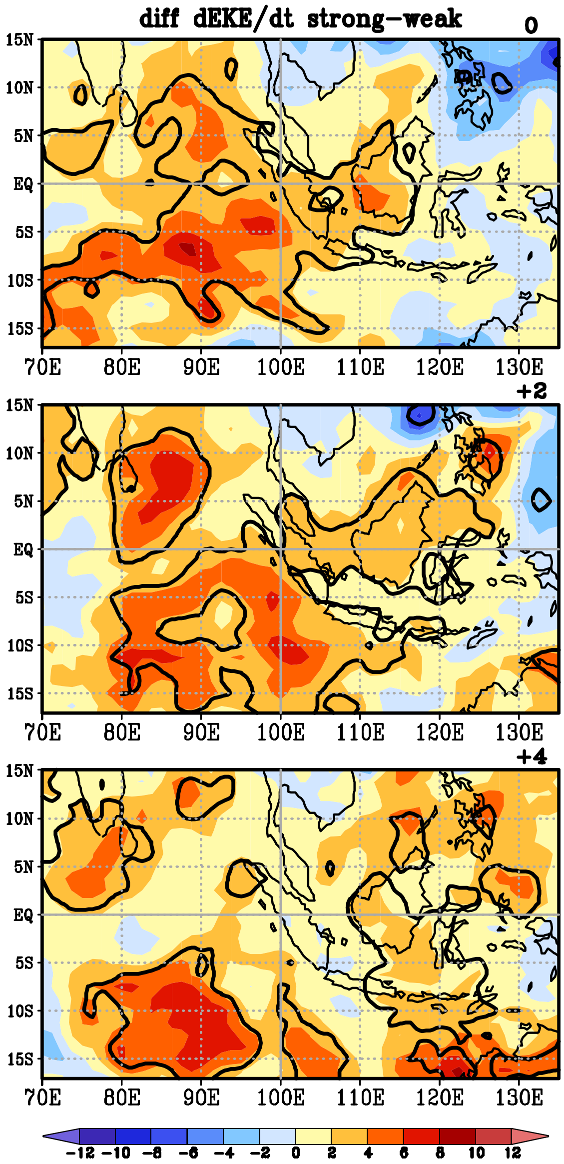

Fig. 9 Differences of composite dK'/dt at 850 hPa between the strong and weak diurnal events. Positive values represent larger dK'/dt for the strong diurnal events. Contours indicate more than the 95% confidence level using the two-sample Student's t test.

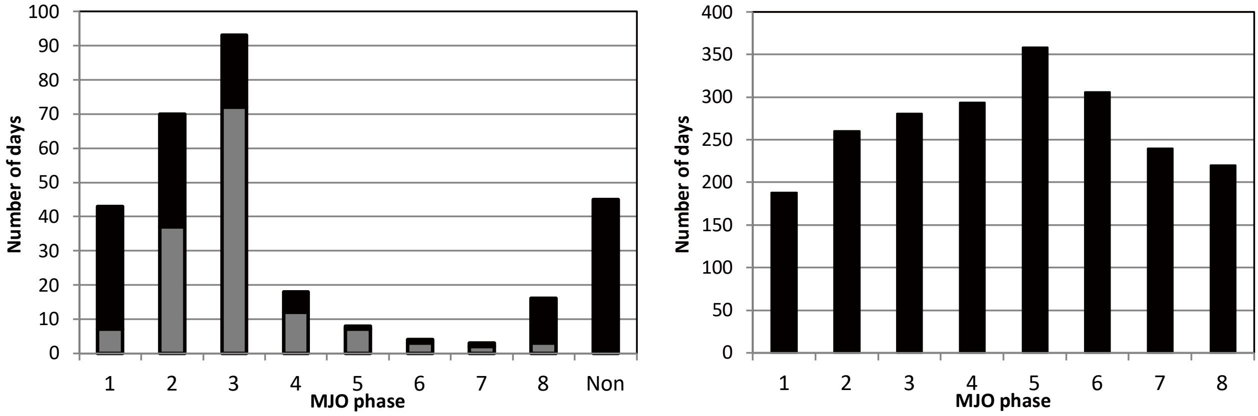

Fig. 10 (left) Accumulated days for the strong diurnal events in each MJO phase. Black bars indicate the days when the MJO amplitude exceeds 1.0, and gray bars represent the days during the MJO events defined in this study when the MJO amplitude exceeds 1.0 for consecutive 15 days. The “Non” refers to the MJO inactive days (see Section 2). (right) Total number of days for each MJO phase when the MJO amplitude exceeds 1.0 during the rainy season.

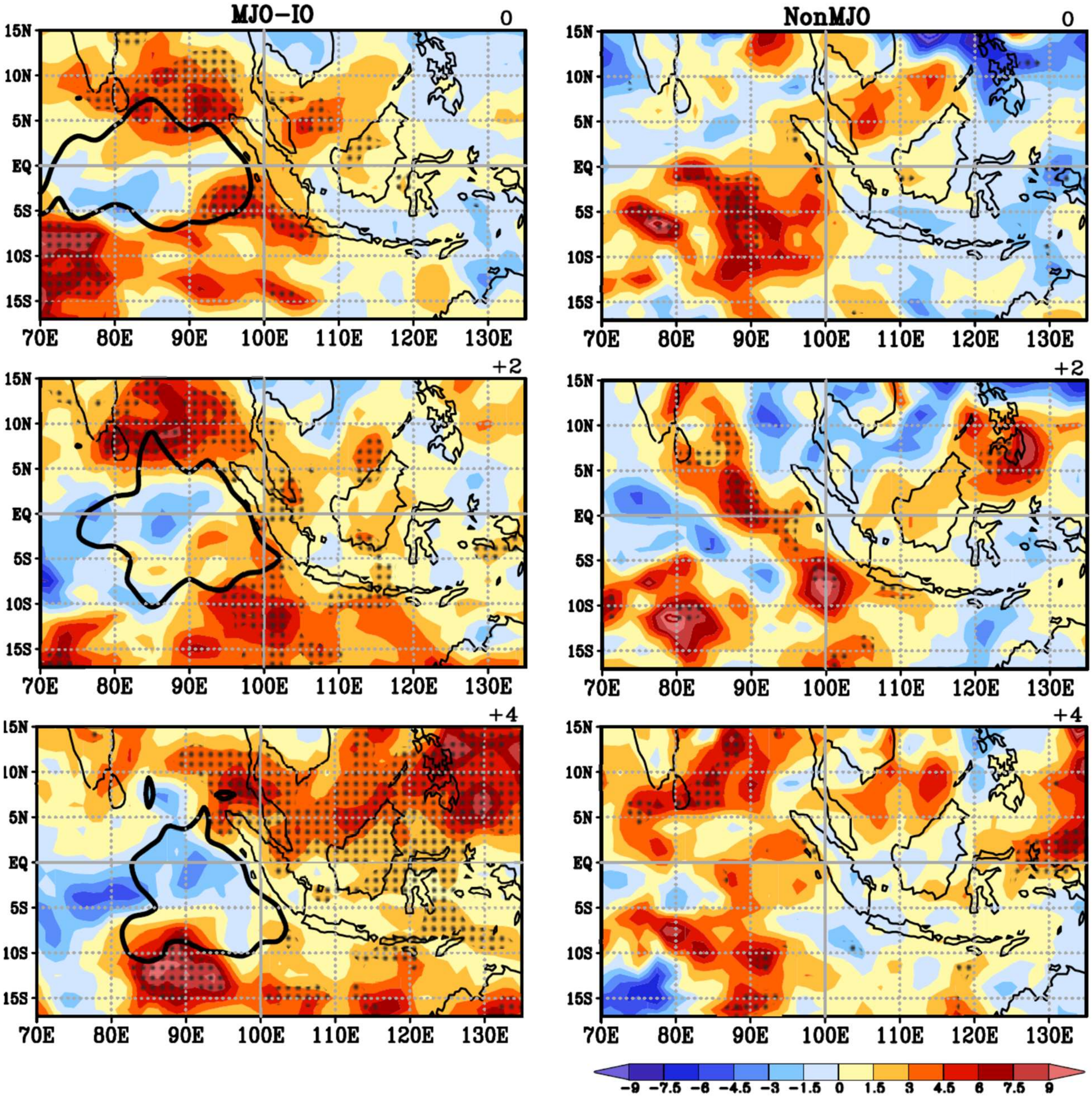

Fig. 11 The composite dK'/dt at 850 hPa (10^{-5} m^2s^{-3}) for the strong diurnal events during (left) the MJO-IO and (right) Non-MJO. Dotted areas represent more than the 95% confidence level. Thick black lines show 20–100 days bandpass-filtered OLR of −20 Wm^{-2}. The numbers on the top right sides show lags in days from the reference day (i.e., day 0).

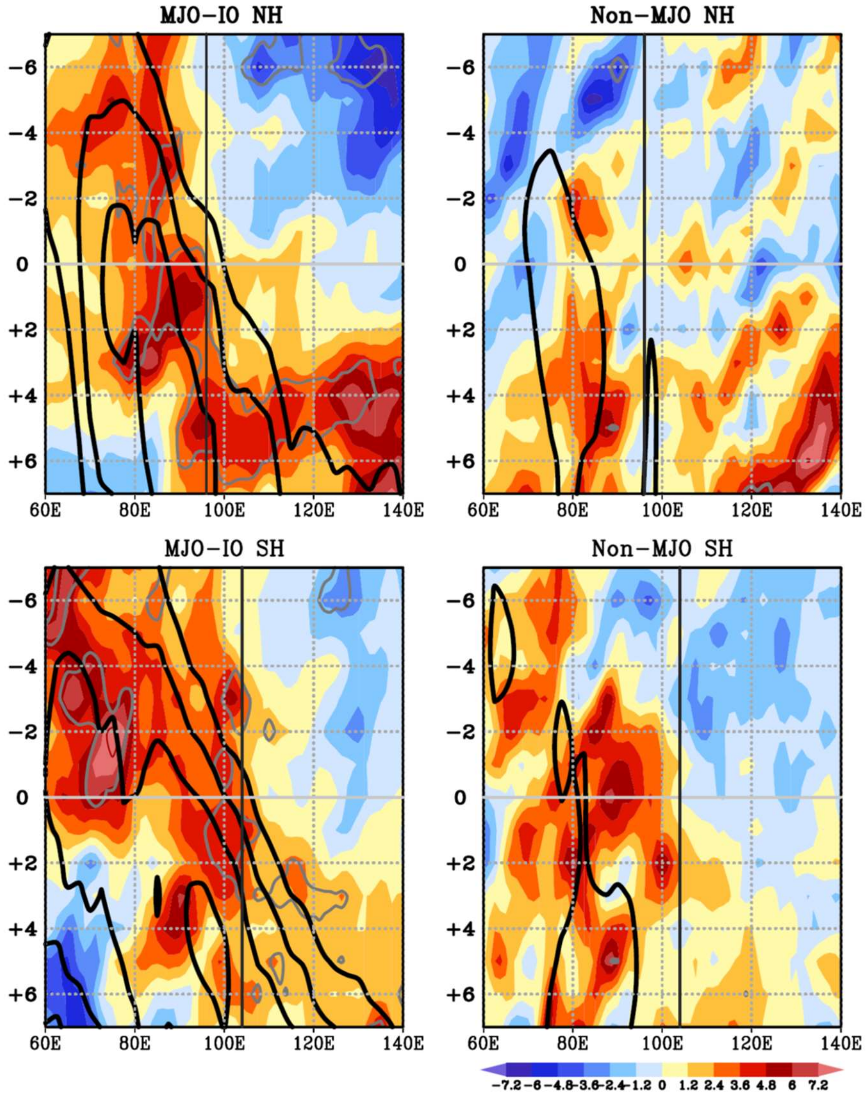

Fig. 12 Same as Fig. 8 except for the strong diurnal events during (left) the MJO-IO and (right) Non-MJO. Thick black lines show negative values of 20–100 days bandpass-filtered OLR with intervals of 5.0 Wm^{-2}.

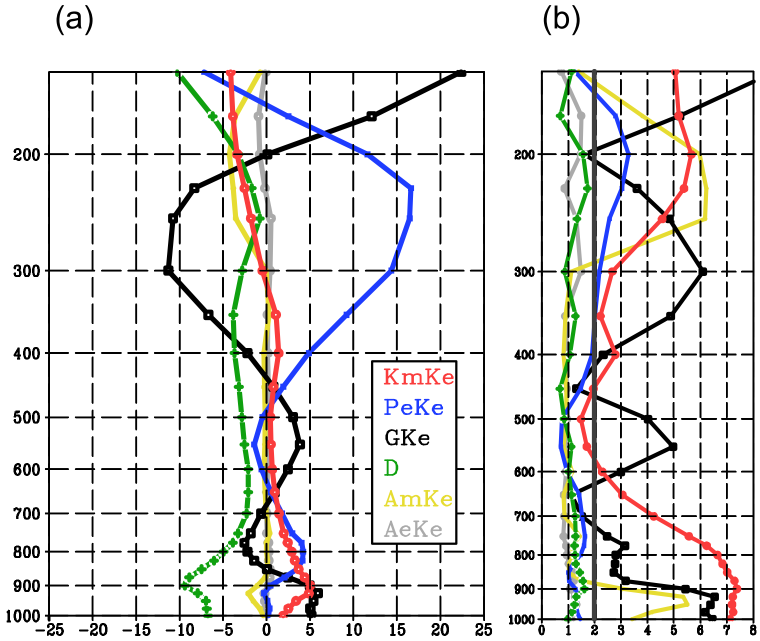

Fig. 13 Composite vertical structures of each term (10^{-5} m^2 s^{-3}) in (a) the eddy kinetic energy budget and (b) Student's t statistics from 1000 to 150 hPa for all the strong diurnal events on day 0 averaged over the southeastern Indian ocean (1.25–6.25S, 92.5–102.5E). The dark gray line in (b) indicates the 95% confidence level.

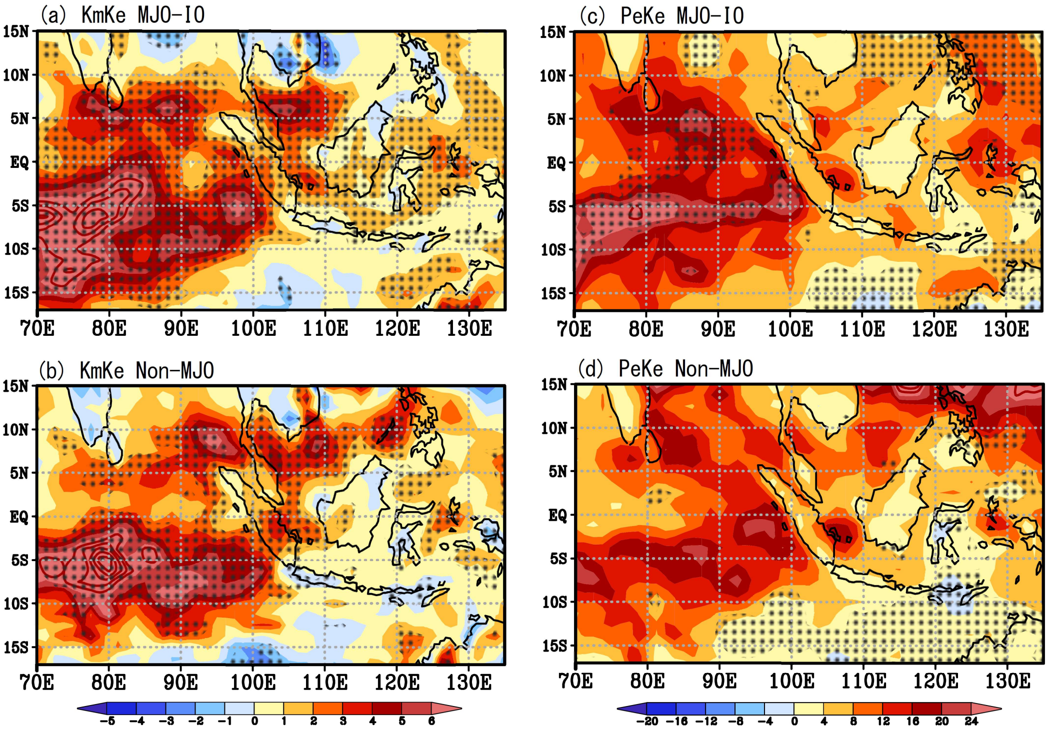

Fig. 14 (a, b) Composite KmKe at 850 hPa (10^{-5} m^2 s^{-3}) and (c, d) PeKe at 250 hPa (10^{-5} m^2 s^{-3}) for the strong diurnal events during (a, c) the MJO-IO and (b, d) Non-MJO on day 0. Dotted areas represent more than the 95% confidence level.

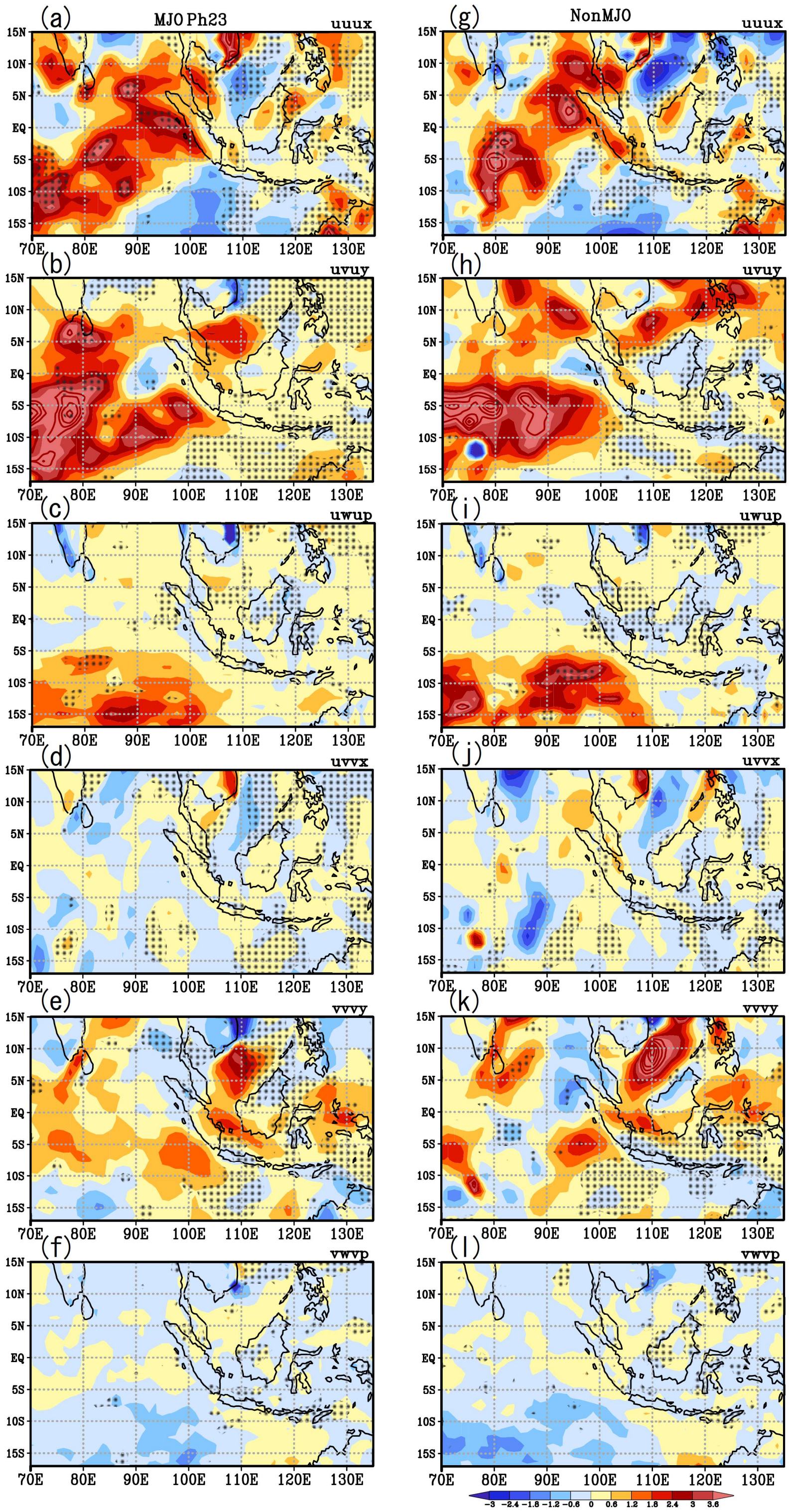

Fig. 15 Composites of each term composing KmKe at 850 hPa (10^{-5} m^2 s^{-3}) for the strong diurnal events during (a-f) the MJO-IO and (g-l) Non-MJO on day 0. Dotted areas represent more than the 95% confidence level.

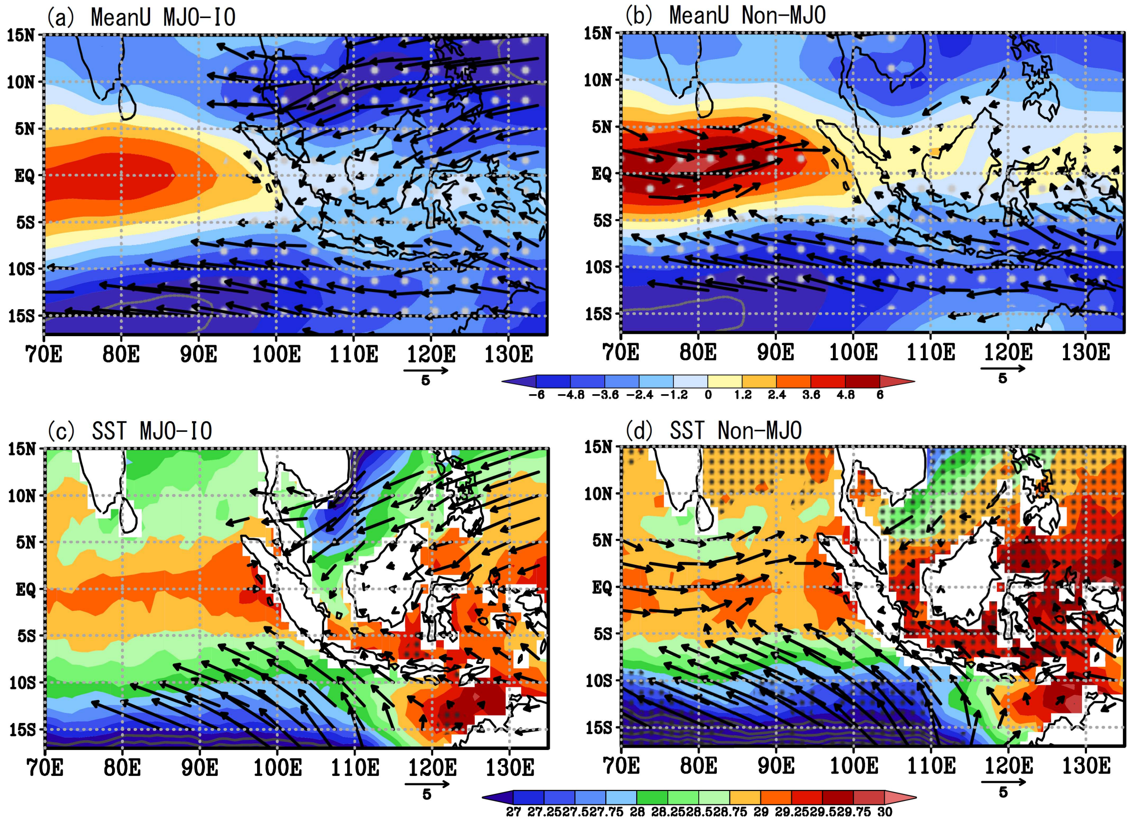

Fig. 16 (a, b) Composite mean zonal winds at 850 hPa (m s^{-1}) and (c, d) SST (°C) for the strong diurnal events during (a, c) the MJO-IO and (b, d) Non-MJO on day 0. Dotted areas represent more than the 95% confidence level. The vectors indicate the composite mean wind fields at (a, b) 850 hPa and (c, d) 1000 hPa, where either the zonal or the meridional component is significant at the 95% level.

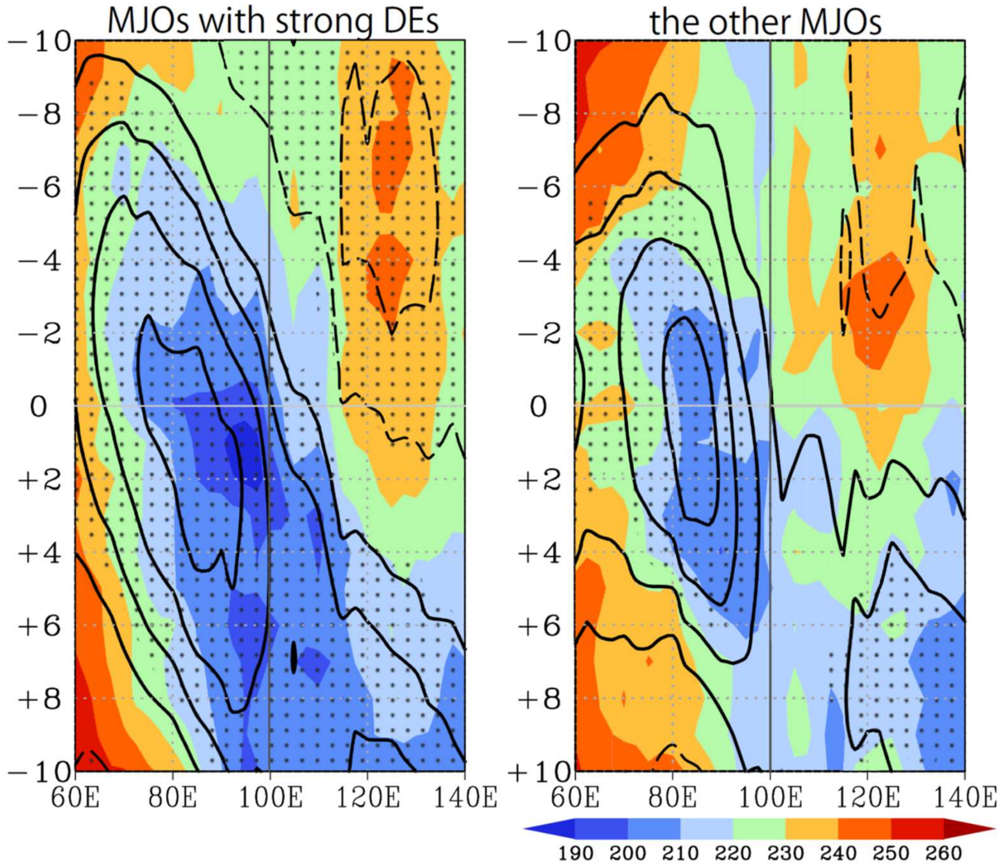

Fig. 17 Time-longitude sections of composite equatorial OLR (shading) and 20–100 days bandpass-filtered OLR (contours) averaged between 10°S and 10°N for (left) the MJO events with the strong diurnal events and (right) the other MJO events. All MJO events have phase 2 and/or 3. Solid (dashed) contours indicate negative (positive) values with intervals of 5.0 Wm^{-2}. Day 0 indicates the last day of the phase 2 or the first day of the phase 3. Dotted areas represent more than the 95% confidence level of composite bandpass-filtered OLR.

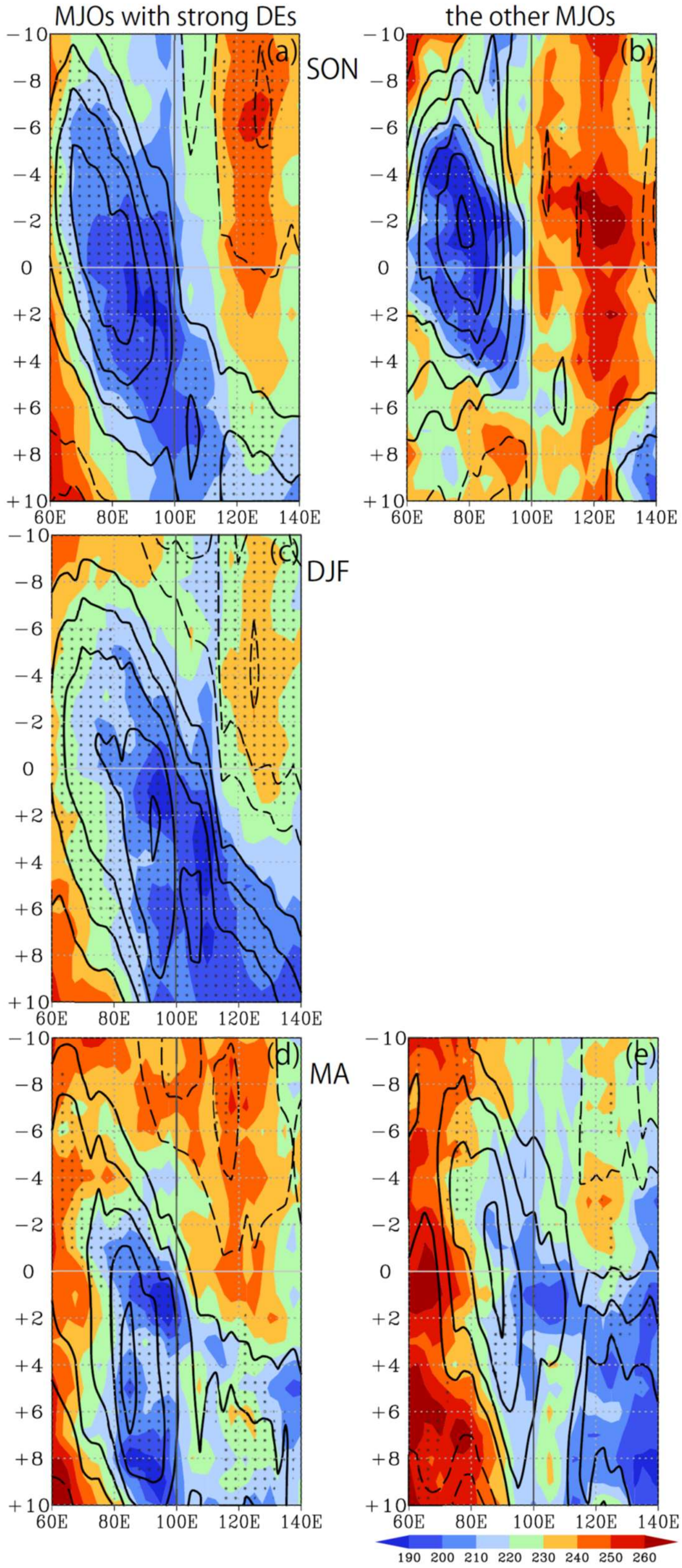

Fig. 18 Same as Fig. 17 except for the MJO events during (a, b) SON, (c) DJF, and (d, e) MA on day 0. Note that composites for the other MJO events during DJF are not shown due to only one sample.

List of Tables

Table 1 The number, averaged duration (days), averaged first phase, and averaged last phase of the MJO events with the strong diurnal events and the others. All MJO events have the phase 2 and/or 3. The duration indicates the number of days when the RMM index meets the definition of the MJO events in this study (see section 2 for the definition).

Table 2 Average duration in each phase of the MJO events with the strong diurnal events and the others.

Table 3 The numbers of the MJO events with the strong diurnal events and the others during SON, DJF, and MA. The averaged numbers per month are shown in parentheses.

	Num.	Ave. Duration	Ave. first PH	Ave. last PH
W/ strong DEs	30	30.4	1.7	6.5
The others	10	24.6	1.9	6.1

Table 1 The number, averaged duration (days), averaged first phase, and averaged last phase of the MJO events with the strong diurnal events and the others. All MJO events have the phase 2 and/or 3. The duration indicates the number of days when the RMM index meets the definition of the MJO events in this study (see section 2 for the definition).

	P1	P2	P3	P4	P5	P6	P7	P8
W/ strong DEs	2.0	5.1	6.0	4.6	5.0	3.3	2.4	2.0
The others	2.2	3.0	4.0	5.8	3.2	2.1	2.1	2.2

Table 2 Average duration in each phase of the MJO events with the strong diurnal events and the others.

	SON	DJF	MA
W/ strong DEs	11 (3.7)	13 (4.3)	6 (3.0)
The others	3 (1.0)	1 (0.3)	6 (3.0)

Table 3 The numbers of the MJO events with the strong diurnal events and the others during SON, DJF, and MA. The averaged numbers per month are shown in parentheses.